Chemical modulation of local transition metal environment enables reversible oxygen redox in Mn-based layered cathodes

Muhammad Mominur Rahman,[1] Scott McGuigan,[1] Shaofeng Li,[2] Lina Gao,[3] Dong Hou,[1] Zhijie Yang,[1] Zhengrui Xu,[1] Cheng-Jun Sun,[4] Jue Liu,[5] Xiaojing Huang,[6] Xianghui Xiao,[6] Yong Chu,[6] Sami Sainio,[2] Dennis Nordlund,[2] Xueqian Kong,[3] Yijin Liu,[2] and Feng Lin[1]*

1. Department of Chemistry, Virginia Tech, Blacksburg, VA 24061, USA
2. Stanford Synchrotron Radiation Lightsource, SLAC National Accelerator Laboratory, Menlo Park, CA 94025, USA
3. Department of Chemistry, Zhejiang University, Hangzhou, Zhejiang 310027, China
4. Advanced Photon Source, Argonne National Laboratory, Argonne, IL 60439, USA
5. Oak Ridge National Laboratory, Oak Ridge, TN 37830, USA
6. National Synchrotron Light Source II, Brookhaven National Laboratory, Upton, NY 11973, USA

Email: fenglin@vt.edu

Abstract

Oxygen redox plays a prominent role in enhancing the energy density of Mn-based layered cathodes. However, understanding the factors affecting the reversibility of oxygen redox is nontrivial due to the complicated concurrent structural and chemical transformations. Herein, we show that local Mn–O symmetry induced structural and chemical evolutions majorly dictate the reversibility of oxygen redox of $Na_xLi_yMn_{1-y}O_2$ in Na cells. We find that $Na_xLi_yMn_{1-y}O_2$ with Jahn-Teller distorted MnO_6 octahedra undergoes severe Mn dissolution during cycling, which destabilizes the transition metal layer resulting in poor Li retention and irreversible oxygen redox. Jahn-Teller distortion of MnO_6 octahedra can be suppressed by modulating the local charge of Mn and Mn–O distance through Mg/Ti dual doping. This leads to reduced Mn dissolution resulting in more reversible oxygen redox. Such stabilization significantly improves the electrochemical performance of Mg/Ti dual doped $Na_xLi_yMn_{1-y}O_2$. Through this work, we show that promoting reversible oxygen redox can benefit from structural stabilization at local length scale, and that modifying the chemical environment through doping chemistry is an efficient strategy to promote local structural stability and thus, oxygen redox.

Oxygen redox can break the limited energy density barrier of layered cathodes, which gives opportunities to develop high energy cathode materials for alkali-ion batteries.[1,2] Oxygen redox is widely studied in Li-rich layered oxides ($Li[Li_xTM_{1-x}]O_2$, where TM stands for transition metal ions).[3,4] In Li-rich layered oxides, unhybridized O 2p orbitals form along the Li–O–Li configurations with Li sitting in both transition metal layer and interlayer.[5] These O 2p orbitals are higher in energy than the bonding molecular orbitals but lower in energy than the antibonding molecular orbitals, putting them closer to the Fermi level than the hybridized O 2p states. Hence, the unhybridized O 2p orbitals are redox active in these materials. Similarly, Na–O–Li and Na–O–Mg configurations are created in sodium layered oxides with 3d transition metals upon substitution of some transition metals by Li or Mg.[6,7] O 2p orbitals in these configurations are also unhybridized and thus, redox active.[8]

Development of layered oxide cathodes with oxygen redox has faced many hurdles. One such hurdle is the irreversible oxygen redox, which often leads to many unwanted phenomena such as electrolyte decomposition and gas evolution.[3] The gas evolution can cause the collapse of the crystal structure leading to the formation of cation dense phase.[9,10] Alkali/alkaline ions in the transition metal layer that are responsible for triggering oxygen redox,[11,12] play a dominant role in determining the oxygen redox reversibility. Bruce and coworkers have shown that Li loss from the transition metal layer of $Na_xLi_yMn_{1-y}O_2$ at high states of charge leads to the formation of underbonded oxygen ions causing O_2 and CO_2 evolution.[12] Many studies have shown that local Li environment in the transition metal layer of Li-substituted Na layered oxides can be in dynamic evolution between the transition metal layer and the interlayer at different stages of cycling.[12–14] The interlayer space provides open channels for Li transport out of the material, leading to Li loss. Hence, enhancing the reversibility of local Li environment is a key factor for stabilizing oxygen

redox. In addition, local transition metal environment provides challenges that can compound the instability issues related to the local Li environment. Local structural distortion surrounding transition metal ions causes lattice stress development, which is detrimental to the electrochemical performance.[15] Mn containing layered oxides often show Jahn-Teller distortion[15] and such distortion aggravates Mn dissolution from the cathode.[16] The accelerated Mn dissolution may cause Li loss and degradation of the transition metal layer that can negatively impact the reversibility of oxygen redox. Doping chemistry has been widely utilized to suppress Jahn-Teller distortion. For example, Mg doping enhances the phase stability through breaking the alkali ion/vacancy ordering and suppress Jahn-Teller distortion through raising the local charge of Mn ions.[17–19] Ti doping can suppress Jahn-Teller distortion through reducing the bond length variation along the axial and equatorial directions.[15,20] Ti dopant is also known to enhance oxygen retention in layered oxides due to its strong chemical bonding with oxygen.[21,22] Such structural stabilization through doping chemistry may also be beneficial towards the reversibility of the oxygen redox process. Hence, a well-informed connection between the role of local structural reversibility of Mn and Li and that of oxygen redox may lead to the stabilization of oxygen redox in Mn-based layered cathodes.

In this study, we show a direct correlation between the local Mn and Li environment and oxygen redox. We utilize Mg/Ti dual dopants on $Na_xLi_yMn_{1-y}O_2$ as a tool to impart the local Mn structural stability. Our study on $Na_xLi_yMn_{1-y}O_2$ and Mg/Ti dual doped $Na_xLi_yMn_{1-y}O_2$ shows that Mg/Ti dual doping can suppress Jahn-Teller distortion and make the local Mn environment more reversible during electrochemical cycling. Such local structural reversibility of Mn leads to suppressed Mn dissolution, stabilizing the Mn layer. This results in stabilization of local Li environment and better overall Li retention. The combined reversibility of the local Mn and Li

environment enhances the stability of oxygen redox in Mg/Ti dual doped $Na_xLi_yMn_{1-y}O_2$, which significantly improves the electrochemical performance in Na cells.

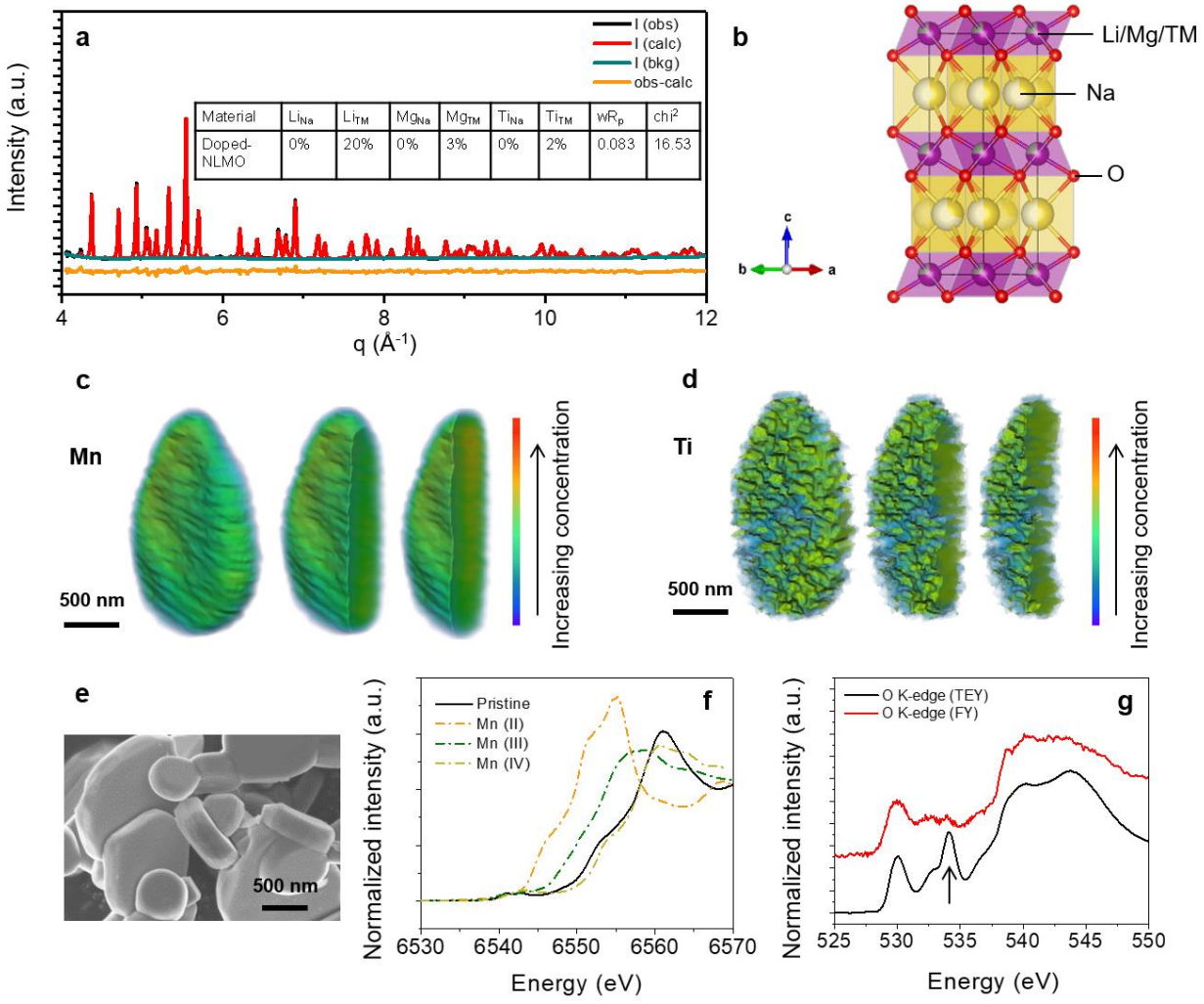

Figure 1. Physicochemical characterization of the pristine $Na_{0.8}Li_{0.2}Mg_{0.03}Ti_{0.02}Mn_{0.75}O_2$ (doped-NLMO). (a) Neutron diffraction pattern with Rietveld refinement. The pattern is refined with a $P6_3/mmc$ space group to figure out the preferred lattice sites the dopants (Mg and Ti), and other elements (Li, and Mn) occupy. The table in the inset shows the occupancy of the elements in either the transition metal layer (TM) or the interlayer (Na) of the crystal structure shown in b. (b) Crystal structure of $Na_{0.8}Li_{0.2}Mg_{0.03}Ti_{0.02}Mn_{0.75}O_2$ showing the lattice sites various elements

(Li, Mg, Ti, Mn, Na, and O) prefer to occupy. TM in the structure stands for transition metals (Mn or Ti). (c) 3D fluorescence tomograph of Mn. The color bar shows the relative distribution of Mn in each voxel. (d) 3D fluorescence tomograph of Ti. The color bar shows the relative distribution of Ti in each voxel. (e) SEM image of the pristine particles of $Na_{0.8}Li_{0.2}Mg_{0.03}Ti_{0.02}Mn_{0.75}O_2$. (f) Mn K-edge XANES spectra of $Na_{0.8}Li_{0.2}Mg_{0.03}Ti_{0.02}Mn_{0.75}O_2$ in the pristine state. The spectra with dotted lines are for Mn in +2 (MnO), +3 (Mn_2O_3), and +4 (MnO_2) oxidation states. (g) O K-edge XAS spectra in total electron yield (TEY) mode and fluorescence yield (FY) mode for pristine $Na_{0.8}Li_{0.2}Mg_{0.03}Ti_{0.02}Mn_{0.75}O_2$. The peak marked by the arrow originates due to the presence of carbonate and/or bicarbonate species.

$Na_xLi_yMn_{1-y}O_2$ is synthesized through a solid-state synthesis method. The phase purity of the material depends closely on the ratio of Na and Li, indicating that Na and Li have a limited solubility (Figure S1). An excess of Li above the solubility leads to the formation of Li_2MnO_3 phase. An excess of Na above the solubility leads to the formation of Na_3MnO_4 phase, in line with reports by Komaba and coworkers (Figure S1).[23] By tuning the composition to $Na_{5/6}Li_{1/4}Mn_{3/4}O_2$ (mentioned as NLMO hereafter), a phase pure P2-type layered oxide can be obtained (Figure S2). Mg/Ti dual doped $Na_xLi_yMn_{1-y}O_2$ is synthesized through a coprecipitation method followed by high temperature calcination (details in the materials and methods section). By tuning the composition ($Na_{0.8}Li_{0.2}Mg_{0.03}Ti_{0.02}Mn_{0.75}O_2$; mentioned as doped-NLMO hereafter) and calcination condition (850 ºC for 10 hours followed by natural furnace cooling), a phase pure material with P2-type crystal structure can be obtained (Figure S3). Crystal structure of both materials can be defined by a hexagonal lattice with $P6_3/mmc$ space group, isostructural to P2-Na_xCoO_2 (Figure S4).[24] An additional reflection is observed in the patterns which indicates Li/Mn honeycomb ordering in the transition metal layer (corresponding to (1/3 1/3 1) crystal plane in

Figure S4).[12,23] Rietveld refinement on neutron diffraction patterns is performed to figure out the specific lattice sites the constituent elements prefer to occupy (Figure 1a and Figure S2). Our refinement shows that both Mg and Ti share occupancy with Mn in the transition metal layer (Figure 1b and Table S1). While all Li sits in the transition metal layer in doped-NLMO (Figure 1b and Table S1), 5% Li sits in the Na layer in NLMO (Table S1). Dopant distribution in doped-NLMO is performed through scanning electron microscopy-energy dispersive X-ray spectroscopy (SEM-EDS images in Figure S5) and 3D fluorescence tomography (Figure 1c and 1d). SEM-EDS is performed on bulk exposed doped-NLMO particles. The bulk of the particles are exposed through a polishing method (details in the materials and methods section). The SEM-EDS images on multiple particles of doped-NLMO show that both Mg and Ti are present throughout the particles (Figure S5). This is further supported by the 3D fluorescence tomographs of Mn and Ti (Figure 1c and 1d) which show that Ti is present within the entire individual particle. The 3D distribution of Ti on the individual particle is somewhat heterogeneous (Figure 1d), which is similar to Ti distribution in Li layered oxides.[17,25] However, Ti shares the same lattice site with Mn, Mg, and Li to form a single phase P2-type crystal structure (Figure 1a and 1b). We have not reported the fluorescence tomograph of Mg because of significant self-absorption of Mg fluorescence signal. Particles of NLMO and doped-NLMO have random to hexagonal plate type morphology (Figure S6 and Figure 1e). The bulk oxidation state of Mn in doped-NLMO is evaluated through hard X-ray absorption spectroscopy (Figure 1f). The bulk oxidation state of Mn is little lower than +4 as can be observed by comparing the edge region of Mn K-edges in Figure 1f. This is consistent with the oxidation state determined from the molecular formula of doped-NLMO (+3.81). Meanwhile, the oxidation state of Mn in NLMO is little lower than +4 (Figure S7), which is also consistent with the calculated oxidation state from the molecular formula of

NLMO (+3.89). The chemical environment of oxygen is probed through O K-edge spectra in total electron yield (TEY) mode and fluorescence yield (FY) mode. At the pristine state, O K-edge shows a pre-edge feature (at around 530 eV-533 eV) originating from the transition of electrons from O 1s orbital to the vacant states of the TM 3d–O 2p hybridized orbitals (Figure 1g). Surface region shows carbonate species, which decreases at the subsurface region of the doped-NLMO particle (compare the intensity of the peak marked by an arrow in Figure 1g).

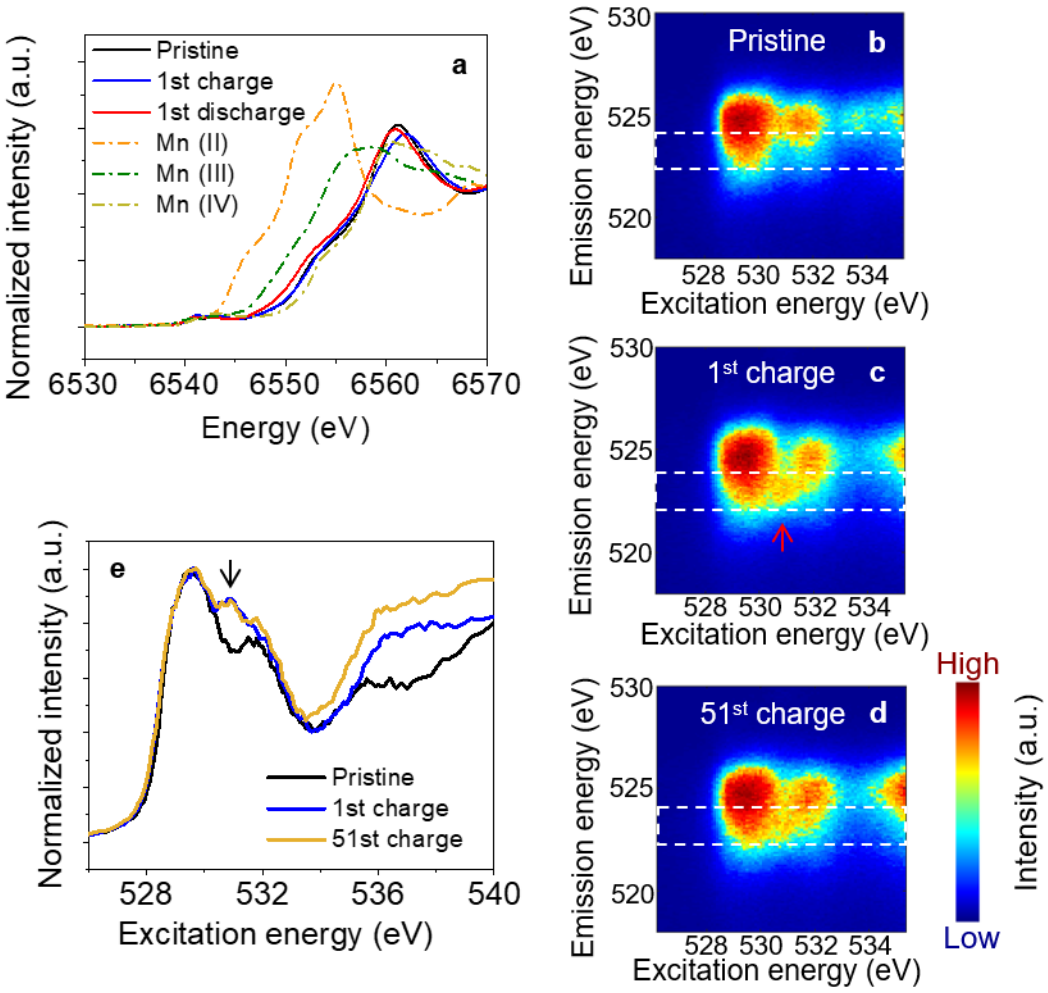

Figure 2. Charge compensation mechanism of $Na_{0.8}Li_{0.2}Mg_{0.03}Ti_{0.02}Mn_{0.75}O_2$ (doped-NLMO) during electrochemical cycling. (a) Mn K-edge XANES spectra in the first cycle (pristine, first charge to 4.5 V, and first discharge to 1.5 V). Cycling is performed at C/10 rate. The dotted spectra

are for standard Mn K-edges at +2 (MnO), +3 (Mn_2O_3), and +4 oxidation states (MnO_2). Oxygen K-edge resonant inelastic X-ray scattering (RIXS) map at (b) pristine state, (c) 1st charge, and (d) 51st charge. The color bar shows the intensity of the emitted photons in arbitrary units. 1st charge is performed at C/10 rate. Subsequent cycling is performed at 1C rate followed by 51st charge at C/10 rate. The red arrow in Figure 2c indicates the signal originating due to oxygen redox. (e) Excitation spectra of the RIXS maps in (b-d). The excitation spectra are derived from the integration of the signal in the vertical direction on the boxed region of RIXS maps in (b-d).

To determine the role of oxygen redox in the charge/discharge process, it is important to understand the detailed charge compensation mechanism during electrochemical cycling. Mn K-edge XANES spectra are collected during the first cycle of doped-NLMO and NLMO at C/10 rate (Figure 2a and Figure S7). The small blueshift on the edge region of the Mn K-edge during the charging process indicates that there is little oxidation of Mn during the first charge of both NLMO (Figure S7) and doped-NLMO (Figure 2a). This indicates that oxygen must be redox active during the charge and discharge process because there is no other redox active transition metal in the material. To monitor the oxygen redox process, oxygen K-edge resonant inelastic X-ray scattering (RIXS) maps are collected at the charged states of doped-NLMO and NLMO (Figure 2b-d and Figure S8). O K-edge RIXS has become the tool of choice to ascertain oxygen redox.[26] RIXS maps can differentiate the signal due to the lattice oxygen redox through resolving the energy of the emitted photons against the excitation energy.[27,28] Such resolution has revealed a unique signal at around 523.7 eV emission energy against a 531eV excitation energy (marked by the red arrow within the white boxed region of Figure 2c). This signal has been revealed to originate from the oxidation of lattice oxygen during the charging process.[29] O K-edge RIXS maps of the charged (4.5 V) doped-NLMO shows a clear signal due to the lattice oxygen redox (marked by the red

arrow in Figure 2c) which is not present in the pristine state (Figure 2b). This proves the participation of lattice oxygen towards redox reaction during cycling. We also utilize O K-edge RIXS to probe the reversibility of oxygen redox in NLMO and doped-NLMO. After 51st charge, the signal of oxygen redox is still present in the O K-edge RIXS map of doped-NLMO (Figure 2d). Excitation spectra derived from integrating the signal along the excitation energy regime on the boxed region in Figure 2b-2c show an increased intensity at 531 eV excitation energy (marked by the black arrow in Figure 2e) on 1st charge to 4.5 V. That increased intensity is still maintained after 51st charge (Figure 2e), indicating a reversible oxygen redox process. However, one can notice a slightly weaker signal due to oxygen redox in NLMO after comparing the O K-edge RIXS maps of 51st charge doped-NLMO and NLMO (Figure S8a-b). The intensity of the spectral feature at 531 eV is also decreased at 51st charge of NLMO in comparison to doped-NLMO (Figure S8c). Overall, our detailed charge compensation study shows that lattice oxygen takes part in redox reactions in both materials and the oxygen redox is more reversible in doped-NLMO than the undoped counterpart.

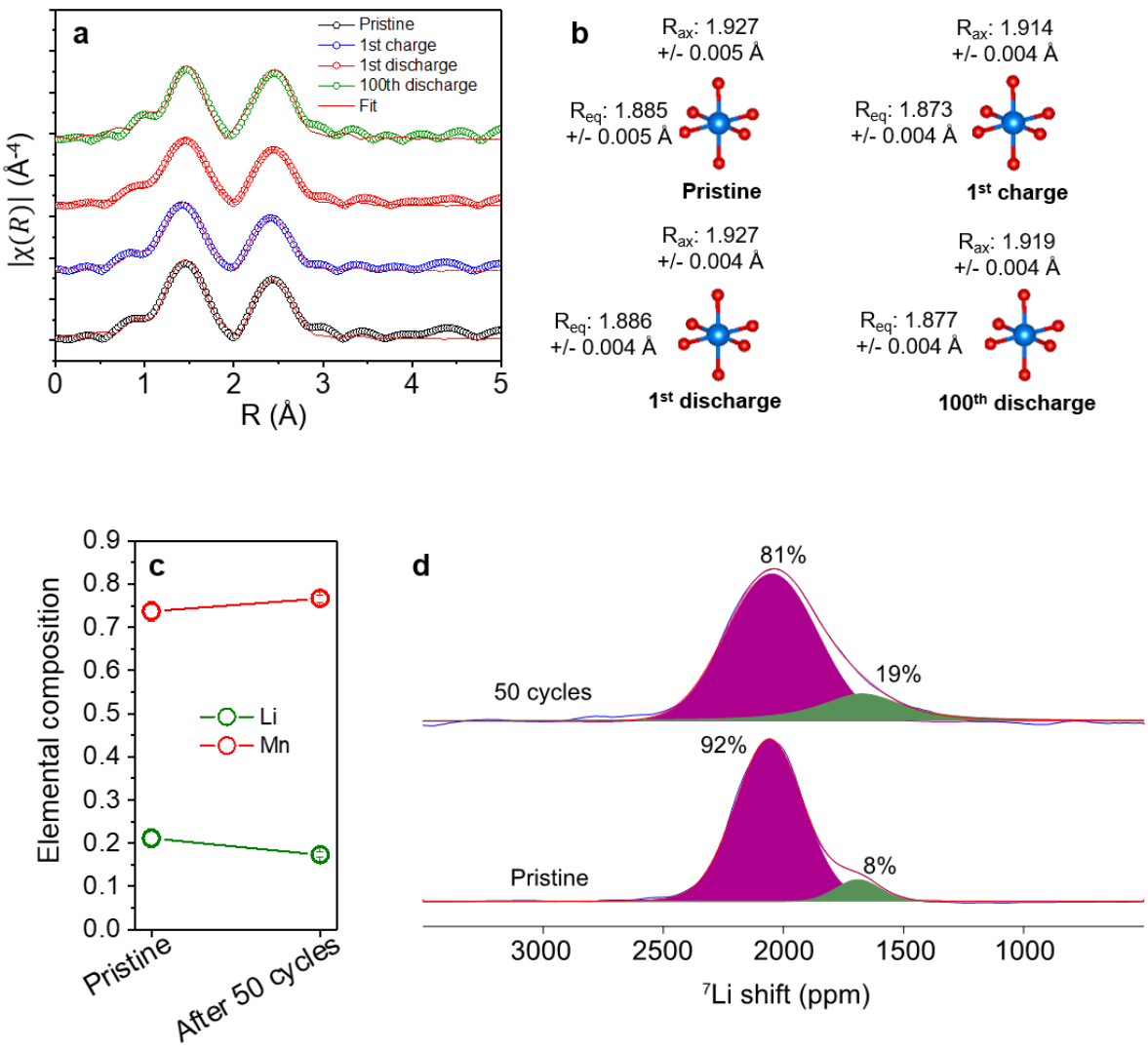

Figure 3. Local Mn and Li structural evolution in $Na_{0.8}Li_{0.2}Mg_{0.03}Ti_{0.02}Mn_{0.75}O_2$ (doped-NLMO) during initial and long-term cycling. (a) Magnitude of the fitted Fourier transformed Mn K-edge EXAFS spectra at different stages of cycling. The cycling is performed at C/10 rate. (b) The evolution of Mn–O distances during different stages of cycling determined from the EXAFS fitting in Figure 3a. R_{eq} represents four Mn–O distances in the equatorial direction of the MnO_6 octahedron. R_{ax} represents two Mn–O distances in the axial direction of the MnO_6 octahedron. Red spheres are for oxygen while the blue spheres are for Mn. (c) Quantification of Li in the material through ICP-MS in the pristine state and after 50 cycles. The cycling is performed

at C/5 rate. The error bars are included with the data points. (d) ^{7}Li pj-MATPASS NMR spectra in the pristine state and after 50 cycles. The cycling is performed at C/5 rate.

We study the local Li and Mn structural evolution in detail to rationalize the observed oxygen redox reversibility in doped-NLMO. Magnitude of the Fourier transformed Mn K-edge extended X-ray absorption fine structure (EXAFS) spectra shows two main peaks (Figure 3a). The peak at around 1.5 Å originates due to the single scattering of photoelectrons by nearest neighboring oxygen scatterer. The peak at around 2.5 Å originates due to the single scattering of photoelectrons by either Mn or Li scatterer in NLMO or Mn, Ti, Mg, or Li scatterer in doped-NLMO. However, the scattering intensity from Li is negligible due to the lighter mass of Li. We perform fitting on the magnitude of the Fourier transformed Mn K-edge EXAFS spectra of NLMO (Figure S9). The fitting shows an elongation in Mn–O bond length along the axial direction and contraction along the equatorial direction in the pristine state and after long term cycling (Figure S9 and Table S2). Jahn-Teller distorted MnO_6 octahedra are reported to be detrimental to the electrochemical performance, leading to Mn dissolution because of the more basic nature of the elongated axial Mn–O bond.[16] Indeed, NLMO has much larger Mn dissolution in comparison to doped-NLMO on electrochemical cycling (Figure S10 and Table S3). The instability of the transition metal layer originating from Jahn-Teller distortion and Mn dissolution also leads to Li loss from NLMO upon long term cycling (66.6% retention after 50 cycles at C/5 rate in Figure S11). Simultaneous loss of both Li and Mn from the transition metal layer can lead to the deterioration of the transition metal layer and formation of severely underbonded oxygen ions, which can impact the reversibility of oxygen redox. Dahn and coworkers reported the formation of underbonded oxygen ions due to the loss of Li from $Na_xLi_yMn_{1-y}O_2$, leading to irreversible oxygen redox.[12] However, doping with Mg and Ti in doped-NLMO effectively suppresses Jahn-

Teller distortion and makes the local MnO_6 evolution more reversible on electrochemical cycling (Figure 3a). Mn–O distance determined through the fitted Fourier transformed Mn K-edge EXAFS spectra shows that Jahn-Teller distortion in MnO_6 octahedra is suppressed in the pristine state (Figure 3a-b and Table S4). The evolution of the MnO_6 octahedra is also reversible on long term electrochemical cycling. The suppression of Jahn-Teller distortion can originate from the cooperative effect of Mg and Ti doping. Mg doping can locally enhance the charge of Mn, reducing Jahn-Teller distortion. Ti doping can reduce the Mn–O bond length variations along the axial and equatorial directions, leading to the suppression of Jahn-Teller distortion.[20] Ti can also strengthen the transition metal (TM)–O bond through decreasing covalency which can enhance oxygen retention.[21,22] This leads to a reversible local Mn structural evolution in doped-NLMO. Suppressing Jahn-Teller distortion leads to less Mn dissolution on long-term cycling of doped-NLMO (Figure S11 and Table S3). Such reduced Mn dissolution will inevitably stabilize the transition metal layer and global Li retention on long term cycling is also improved in comparison to NLMO as a result (81.8% Li retention after 50 cycles at C/5 rate in Figure 3c). We probe the local Li environment in doped-NLMO closely with ^{7}Li projection magic angle turning-phase adjusted sideband separation (pj-MATPASS) NMR. The spectra show a major peak at a chemical shift bit larger than 2000 ppm with a small shoulder on the lower chemical shift (Figure 3d). The major peak originates for the Li surrounded by 6 Mn ions. The shoulder forms when in addition to Mn, Li is also surrounded by Ti or Mg.[30] No accumulation of Li in the interlayer is observed from the ^{7}Li NMR spectra in the pristine state and after long term cycling as there is no peak lower than 1000 ppm chemical shift in Figure 3d.[12] Therefore, for both pristine and 50 cycles, the main peak and the shoulder in the NMR spectra (Figure 3d) can be accounted for Li sitting on the transition metal layer. Even after long term cycling, all Li can still be found in the transition metal layer with

no accumulation of Li in the interlayer. Meanwhile, many studies show the accumulation of Li in the interlayer space of Li substituted Na layered oxides on electrochemical cycling.[13,14] The interlayer space provides an open channel for Li migration out of the material which can cause permanent Li loss on electrochemical cycling. Overall, the stable local Li and Mn environment in doped-NLMO ensures that there is less accumulation of Li in the interlayer. This along with reduced Mn dissolution can stabilize the transition metal layer, which helps sustain oxygen redox on long term cycling. Reversible oxygen redox also leads to stable interfacial chemistry as observed through O K-edge spectra in FY mode. After 100 cycles at C/10, carbonate like species is observed in NLMO whereas no such species can be seen in doped-NLMO (peak marked by the arrow in Figure S12). This indicates a greater decomposition of the electrolyte to form carbonate species on NLMO which can be facilitated by the less reversible oxygen redox in NLMO.[31]

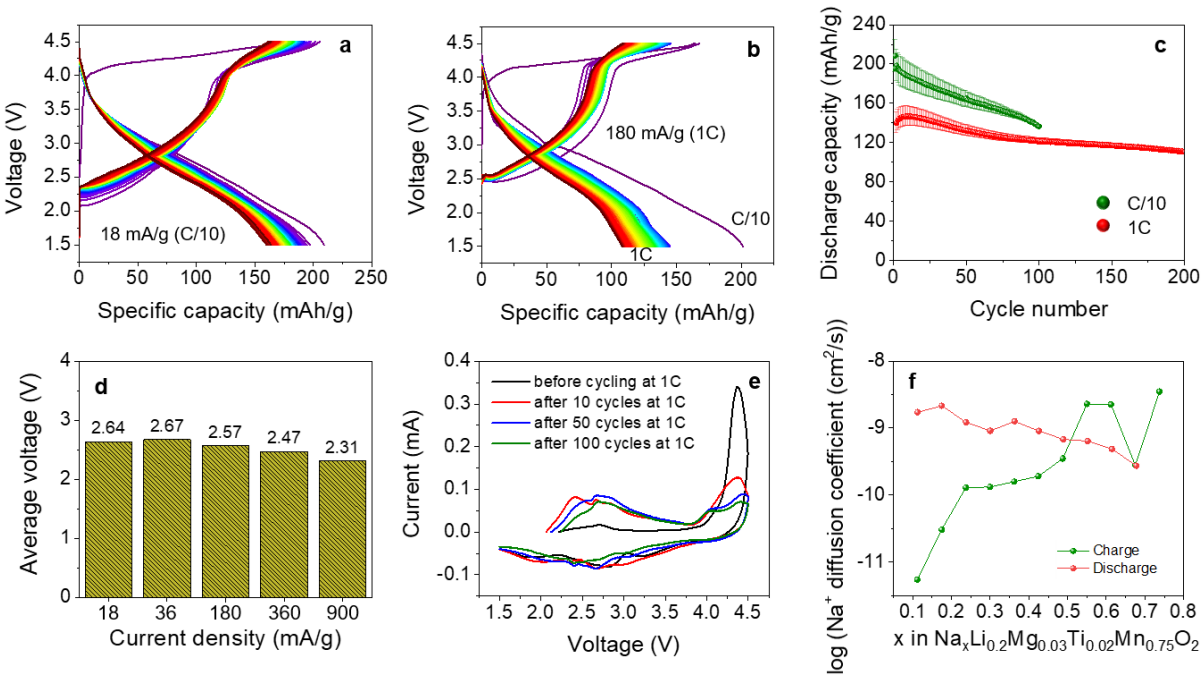

Figure 4. Electrochemical characterization of $Na_{0.8}Li_{0.2}Mg_{0.03}Ti_{0.02}Mn_{0.75}O_2$ (doped-NLMO). (a) Charge and discharge curves of the Na cell containing $Na_{0.8}Li_{0.2}Mg_{0.03}Ti_{0.02}Mn_{0.75}O_2$ as the

cathode material at C/10 rate within the voltage window of 1.5-4.5 V. (b) Charge and discharge curves of Na cell containing $Na_{0.8}Li_{0.2}Mg_{0.03}Ti_{0.02}Mn_{0.75}O_2$ as the cathode material at 1C rate within the voltage window of 1.5-4.5 V. The first cycle is performed at C/10 rate. (c) Capacity retention against cycle numbers at C/10 and 1C rate of $Na_{0.8}Li_{0.2}Mg_{0.03}Ti_{0.02}Mn_{0.75}O_2$ in Na cell. The capacity retentions are averaged from multiple cells. (d) Average voltage at different current densities delivered by $Na_{0.8}Li_{0.2}Mg_{0.03}Ti_{0.02}Mn_{0.75}O_2$. (e) Cyclic voltammogram of $Na_{0.8}Li_{0.2}Mg_{0.03}Ti_{0.02}Mn_{0.75}O_2$ before and after cycling for various cycles at 1C. The scanning is performed at 0.1 mV/s within 1.5-4.5 V. (f) Apparent Na^+ diffusion coefficient calculated from the GITT measurement. GITT measurement is performed at C/10 rate with 1 hour of constant current pulse followed by 10 hours of open circuit relaxation.

Reversible local structural evolution and oxygen redox lead to significant improvement in electrochemical performance of doped-NLMO in comparison to NLMO (Figure 4 and Figure S13). Doped-NLMO delivers an initial discharge capacity of 210 mAh/g at C/10 rate (Figure 4a) and 145 mAh/g at 1C rate (Figure 4b). In comparison, NLMO delivers an initial discharge capacity of 221 mAh/g at C/10 rate (Figure S13a) and 151 mAh/g at 1C rate (Figure S13b). NLMO delivers comparable capacity to similar $Na_xLi_yMn_{1-y}O_2$ materials (similar or different x/y ratios) reported in the literature.[23,32,33] In comparison to NLMO, the capacity retention is substantially improved in doped-NLMO at both C/10 and 1C rate (Figure 4c and Figure S13c). Likewise, energy retention is also stabilized in doped-NLMO (Figure S13d and Figure S14a). A stable Coulombic efficiency is delivered by doped-NLMO (Figure S14b) in comparison to NLMO (Figure S13e). A comparable average voltage is delivered by both materials at C/10 and 1C but more stable average voltage is delivered by doped-NLMO (Figure S13f and Figure S14c). Doping of Mg and Ti in NLMO can also slow down the lowering of the output voltage at faster C-rates (Figure 4d, Figure S13g).

Doped-NLMO delivers an average voltage of 2.57 V at 1C (180 mA/g current density) whereas NLMO delivers 2.25 V average voltage at 1C. Even at 5C (900 mA/g), the average voltage of doped-NLMO (2.31 V) is higher than NLMO at 1C (2.25 V). The CV profile of both materials at 0.1 mV/s scan rate shows a peak at 4.38 V on the direction of positive voltage sweep in the first and second cycle, which can be attributed to high-voltage phase transformation (Figure S13h and Figure S14d).[34] This peak is observed even after cycling for 100 cycles at 1C (Figure 4e) when scanned at the same scanning rate, even though a decrease in peak height can be seen. However, the peak quickly diminishes in NLMO after cycling for just 50 cycles at 1C and replaced by a solvent oxidation peak (Figure S15), indicating an irreversible phase transformation process. The overall improvement of the electrochemical performance and the reversibility of oxygen redox reaction also led to stable interfacial processes in doped-NLMO. Figure S12 shows that NLMO undergoes severe interfacial side reactions with more carbonate-based surface products. This leads to significant development of interfacial charge transfer resistance in NLMO in comparison to doped-NLMO (Figure S13i and Figure S14e).[35] Kinetic measurement is performed through galvanostatic intermittent titration technique (Figure 4f).[36] The apparent Na^+ diffusion coefficient of doped-NLMO during charging ranges from 5.43E-12 to 2.25E-9 cm^2/s (Figure 4f). The diffusion coefficient during the discharge process varies from 9.08E-10 to 1.22E-9 cm^2/s (Figure 4f). Meanwhile, the apparent Na^+ diffusion coefficient of NLMO during the charging process ranges from 2.94E-11 to 3.53E-8 and 1.56E-11 to 1.08E-9 during discharging (Figure S16). Overall, the detailed electrochemical performance evaluation shows that making the local structural evolution more reversible through Mg and Ti dual doping not only leads to stable oxygen redox but also substantially improves the electrochemical performance.

In summary, our work shows the critical role that the local structural environment in the transition metal layer plays to stabilize oxygen redox in Mn-based layered oxide cathodes. Li-substitution in the transition metal layer can trigger oxygen redox due to the formation of unhybridized O 2p orbitals. However, the instability of Li and transition metal in the transition metal layer can make the oxygen redox process less reversible. We probe the local structural environment of Mn in $Na_{5/6}Li_{1/4}Mn_{3/4}O_2$ and observe Jahn-Teller distortion in MnO_6 octahedra through EXAFS analysis. The distortion causes severe Mn dissolution upon long term cycling. The instability of Mn leads to Li loss, an irreversible oxygen redox process, and unstable electrochemical performance. Mn dissolution can be suppressed by reducing the Jahn-Teller distortion through chemical modulation of local Mn environment by Mg and Ti dual doping. Such stabilization of the transition metal layer causes better Li retention and stable local Li environment with no Li accumulation in the interlayer as probed through ^{7}Li pj-MATPASS NMR (no peak at lower than 1000 ppm chemical shift in Figure 3d). As a result, a reversible oxygen redox process is observed through RIXS. Overall, the more reversible local Li and Mn environment and stable oxygen redox significantly improves the electrochemical performance of $Na_{0.8}Li_{0.2}Mg_{0.03}Ti_{0.02}Mn_{0.75}O_2$. This work provides fundamental mechanistic understanding on the interplay between local Li and Mn environments and oxygen redox as well as showcases that stabilizing local environment in the transition metal layer is a promising pathway for stable oxygen redox.

Acknowledgement

The work was supported by the National Science Foundation under no. CBET 1912885, as well as Virginia Tech College of Science Lay Nam Chang Dean's Discovery Fund. Use of the Stanford Synchrotron Radiation Lightsource, SLAC National Accelerator Laboratory, is supported by the U.S.

Department of Energy, Office of Science, Office of Basic Energy Sciences under Contract No. DE-AC02-76SF00515. This research used resources of the Advanced Photon Source; a U.S. Department of Energy (DOE) Office of Science User Facility operated for the DOE Office of Science by Argonne National Laboratory under Contract No. DE-AC02-06CH11357. Use of the resources of the National Synchrotron Light Source II is supported by Department of Energy (DOE), Office of Science User Facility operated for the DOE Office of Science by the Brookhaven National Laboratory under Contract No. DE-SC0012704. A portion of this research used resources at the Spallation Neutron Source, a DOE Office of Science User Facility operated by the Oak Ridge National Laboratory. The authors would like to thank Stephanie Spence for data discussion.

Author contribution

F.L. designed and conceived the project and assisted in manuscript preparation. M.M.R. synthesized materials, performed electrochemical analysis, XRD, XAS, X-ray fluorescence tomography, SEM-EDS data analysis, and manuscript preparation. S.M. assisted in materials synthesis. S.L. and Y.L. acquired and analyzed RIXS data. L.G. and X.K. acquired and analyzed ^{7}Li-NMR data. D.H. analyzed neutron diffraction data. Z.Y., Z.X. and C.S. acquired hard XAS data. J.L. acquired neutron diffraction data. X.H., X.X., and Y.C. acquired fluorescence tomographs. S.S. and D.N. acquired soft XAS data.

Conflict of interest

The authors declare no conflict of interest.

References

(1) Assat, G.; Tarascon, J. M. Fundamental Understanding and Practical Challenges of Anionic Redox Activity in Li-Ion Batteries. *Nat. Energy* **2018**, *3* (5), 373–386.

https://doi.org/10.1038/s41560-018-0097-0.

(2) Rahman, M. M.; Lin, F. Oxygen Redox Chemistry in Rechargeable Li-Ion and Na-Ion Batteries. *Matter* **2021**, *4* (2), 490–527. https://doi.org/10.1016/J.MATT.2020.12.004.

(3) Luo, K.; Roberts, M. R.; Hao, R.; Guerrini, N.; Pickup, D. M.; Liu, Y. S.; Edström, K.; Guo, J.; Chadwick, A. V.; Duda, L. C.; Bruce, P. G. Charge-Compensation in 3d-Transition-Metal-Oxide Intercalation Cathodes through the Generation of Localized Electron Holes on Oxygen. *Nat. Chem.* **2016**, *8* (7), 684–691. https://doi.org/10.1038/nchem.2471.

(4) Koga, H.; Croguennec, L.; Ménétrier, M.; Mannessiez, P.; Weill, F.; Delmas, C. Different Oxygen Redox Participation for Bulk and Surface: A Possible Global Explanation for the Cycling Mechanism of Li1.20Mn 0.54Co0.13Ni0.13O2. *J. Power Sources* **2013**, *236*, 250–258. https://doi.org/10.1016/j.jpowsour.2013.02.075.

(5) Seo, D.-H.; Lee, J.; Urban, A.; Malik, R.; Kang, S.; Ceder, G. The Structural and Chemical Origin of the Oxygen Redox Activity in Layered and Cation-Disordered Li-Excess Cathode Materials. *Nat. Chem.* **2016**, *8* (7), 692–697. https://doi.org/10.1038/nchem.2524.

(6) Maitra, U.; House, R. A.; Somerville, J. W.; Tapia-Ruiz, N.; Lozano, J. G.; Guerrini, N.; Hao, R.; Luo, K.; Jin, L.; Pérez-Osorio, M. A.; Massel, F.; Pickup, D. M.; Ramos, S.; Lu, X.; McNally, D. E.; Chadwick, A. V.; Giustino, F.; Schmitt, T.; Duda, L. C.; Roberts, M. R.; Bruce, P. G. Oxygen Redox Chemistry without Excess Alkali-Metal Ions in Na2/3[Mg0.28Mn0.72]O2. *Nat. Chem.* **2018**. https://doi.org/10.1038/nchem.2923.

(7) Wang, Q. C.; Meng, J. K.; Yue, X. Y.; Qiu, Q. Q.; Song, Y.; Wu, X. J.; Fu, Z. W.; Xia, Y.

Y.; Shadike, Z.; Wu, J.; Yang, X. Q.; Zhou, Y. N. Tuning P2-Structured Cathode Material by Na-Site Mg Substitution for Na-Ion Batteries. *J. Am. Chem. Soc.* **2019**, *141* (2), 840–848. https://doi.org/10.1021/jacs.8b08638.

(8) House, R. A.; Maitra, U.; Pérez-Osorio, M. A.; Lozano, J. G.; Jin, L.; Somerville, J. W.; Duda, L. C.; Nag, A.; Walters, A.; Zhou, K. J.; Roberts, M. R.; Bruce, P. G. Superstructure Control of First-Cycle Voltage Hysteresis in Oxygen-Redox Cathodes. *Nature* **2020**, *577* (7791), 502–508. https://doi.org/10.1038/s41586-019-1854-3.

(9) Boulineau, A.; Simonin, L.; Colin, J.-F.; Bourbon, C.; Patoux, S. First Evidence of Manganese-Nickel Segregation and Densification upon Cycling in Li-Rich Layered Oxides for Lithium Batteries. *Nano Lett.* **2013**, *13* (8), 3857–3863. https://doi.org/10.1021/nl4019275.

(10) Rahman, M. M.; Chen, W. Y.; Mu, L.; Xu, Z.; Xiao, Z.; Li, M.; Bai, X. M.; Lin, F. Defect and Structural Evolution under High-Energy Ion Irradiation Informs Battery Materials Design for Extreme Environments. *Nat. Commun.* **2020**, *11* (1), 4548. https://doi.org/10.1038/s41467-020-18345-4.

(11) Wang, Q.-C.; Meng, J.-K.; Yue, X.-Y.; Qiu, Q.-Q.; Song, Y.; Wu, X.-J.; Fu, Z.-W.; Xia, Y.-Y.; Shadike, Z.; Wu, J.; Yang, X.-Q.; Zhou, Y.-N. Tuning P2-Structured Cathode Material by Na-Site Mg Substitution for Na-Ion Batteries. *J. Am. Chem. Soc.* **2019**, *141* (2), 840–848. https://doi.org/10.1021/jacs.8b08638.

(12) House, R. A.; Maitra, U.; Jin, L.; Lozano, J. G.; Somerville, J. W.; Rees, N. H.; Naylor, A. J.; Duda, L. C.; Massel, F.; Chadwick, A. V.; Ramos, S.; Pickup, D. M.; McNally, D. E.; Lu, X.; Schmitt, T.; Roberts, M. R.; Bruce, P. G. What Triggers Oxygen Loss in Oxygen

Redox Cathode Materials? *Chem. Mater.* **2019**, *31* (9), 3293–3300. https://doi.org/10.1021/acs.chemmater.9b00227.

(13) Yang, L.; Li, X.; Liu, J.; Xiong, S.; Ma, X.; Liu, P.; Bai, J.; Xu, W.; Tang, Y.; Hu, Y.-Y.; Liu, M.; Chen, H. Lithium-Doping Stabilized High-Performance P2–Na $_{0.66}$ Li $_{0.18}$ Fe $_{0.12}$ Mn $_{0.7}$ O $_2$ Cathode for Sodium Ion Batteries. *J. Am. Chem. Soc.* **2019**, *141* (16), 6680–6689. https://doi.org/10.1021/jacs.9b01855.

(14) Xu, J.; Lee, D. H.; Clément, R. J.; Yu, X.; Leskes, M.; Pell, A. J.; Pintacuda, G.; Yang, X.-Q.; Grey, C. P.; Meng, Y. S. Identifying the Critical Role of Li Substitution in P2–Na $_x$ [Li $_y$ Ni $_z$ Mn $_{1-y-z}$]O $_2$ (0 < *x* , *y* , *z* < 1) Intercalation Cathode Materials for High-Energy Na-Ion Batteries. *Chem. Mater.* **2014**, *26* (2), 1260–1269. https://doi.org/10.1021/cm403855t.

(15) Han, M. H.; Gonzalo, E.; Sharma, N.; López Del Amo, J. M.; Armand, M.; Avdeev, M.; Saiz Garitaonandia, J. J.; Rojo, T. High-Performance P2-Phase Na2/3Mn0.8Fe0.1Ti0.1O2 Cathode Material for Ambient-Temperature Sodium-Ion Batteries. *Chem. Mater.* **2016**, *28* (1), 106–116. https://doi.org/10.1021/acs.chemmater.5b03276.

(16) Asl, H. Y.; Manthiram, A. Reining in Dissolved Transition-Metal Ions. *Science (80-.).* **2020**, *369* (6500), 140–141. https://doi.org/10.1126/science.abc5454.

(17) Mu, L.; Zhang, R.; Kan, W. H.; Zhang, Y.; Li, L.; Kuai, C.; Zydlewski, B.; Rahman, M. M.; Sun, C.-J.; Sainio, S.; Avdeev, M.; Nordlund, D.; Xin, H. L.; Lin, F. Dopant Distribution in Co-Free High-Energy Layered Cathode Materials. *Chem. Mater.* **2019**, *31* (23), 9769–9776. https://doi.org/10.1021/acs.chemmater.9b03603.

(18) Huang, Y.; Yan, Z.; Luo, W.; Hu, Z.; Liu, G.; Zhang, L.; Yang, X.; Ou, M.; Liu, W.;

Huang, L.; Lin, H.; Chen, C. Te; Luo, J.; Li, S.; Han, J.; Chou, S.; Huang, Y. Vitalization of P2–Na2/3Ni1/3Mn2/3O2 at High-Voltage Cyclability via Combined Structural Modulation for Sodium-Ion Batteries. *Energy Storage Mater.* **2020**, *29*, 182–189. https://doi.org/10.1016/j.ensm.2020.04.012.

(19) Singh, G.; Gupta, S. L.; Prasad, R.; Auluck, S.; Gupta, R.; Sil, A. Suppression of Jahn-Teller Distortion by Chromium and Magnesium Doping in Spinel LiMn2O4: A First-Principles Study Using GGA and GGA+U. *J. Phys. Chem. Solids* **2009**, *70* (8), 1200–1206. https://doi.org/10.1016/j.jpcs.2009.07.001.

(20) Fang, T.; Guo, S.; Jiang, K.; Zhang, X.; Wang, D.; Feng, Y.; Zhang, X.; Wang, P.; He, P.; Zhou, H. Revealing the Critical Role of Titanium in Layered Manganese-Based Oxides toward Advanced Sodium-Ion Batteries via a Combined Experimental and Theoretical Study. *Small Methods* **2019**, *3* (4), 1800183. https://doi.org/10.1002/smtd.201800183.

(21) Steiner, J. D.; Cheng, H.; Walsh, J.; Zhang, Y.; Zydlewski, B.; Mu, L.; Xu, Z.; Rahman, M. M.; Sun, H.; Michel, F. M.; Sun, C.-J.; Nordlund, D.; Luo, W.; Zheng, J.-C.; Xin, H. L.; Lin, F. Targeted Surface Doping with Reversible Local Environment Improves Oxygen Stability at the Electrochemical Interfaces of Nickel-Rich Cathode Materials. *ACS Appl. Mater. Interfaces* **2019**, *11* (41), 37885–37891. https://doi.org/10.1021/acsami.9b14729.

(22) Cheng, J.; Mu, L.; Wang, C.; Yang, Z.; Xin, H. L.; Lin, F.; Persson, K. A. Enhancing Surface Oxygen Retention through Theory-Guided Doping Selection in Li1-: XNiO2for next-Generation Lithium-Ion Batteries. *J. Mater. Chem. A* **2020**, *8* (44), 23293–23303. https://doi.org/10.1039/d0ta07706b.

(23) Yabuuchi, N.; Hara, R.; Kajiyama, M.; Kubota, K.; Ishigaki, T.; Hoshikawa, A.; Komaba, S. New O2/P2-Type Li-Excess Layered Manganese Oxides as Promising Multi-Functional Electrode Materials for Rechargeable Li/Na Batteries. *Adv. Energy Mater.* **2014**, *4* (13), 1301453. https://doi.org/10.1002/aenm.201301453.

(24) Delmas, C.; Braconnier, J. J.; Fouassier, C.; Hagenmuller, P. Electrochemical Intercalation of Sodium in NaxCoO2 Bronzes. *Solid State Ionics* **1981**, *3–4* (C), 165–169. https://doi.org/10.1016/0167-2738(81)90076-X.

(25) Yang, Z.; Mu, L.; Hou, D.; Rahman, M. M.; Xu, Z.; Liu, J.; Nordlund, D.; Sun, C.; Xiao, X.; Lin, F. Probing Dopant Redistribution, Phase Propagation, and Local Chemical Changes in the Synthesis of Layered Oxide Battery Cathodes. *Adv. Energy Mater.* **2021**, *11* (1), 2002719. https://doi.org/10.1002/aenm.202002719.

(26) Yang, W.; Devereaux, T. P. Anionic and Cationic Redox and Interfaces in Batteries: Advances from Soft X-Ray Absorption Spectroscopy to Resonant Inelastic Scattering. *Journal of Power Sources*. Elsevier B.V. June 15, 2018, pp 188–197. https://doi.org/10.1016/j.jpowsour.2018.04.018.

(27) Zhuo, Z.; Pemmaraju, C. Das; Vinson, J.; Jia, C.; Moritz, B.; Lee, I.; Sallies, S.; Li, Q.; Wu, J.; Dai, K.; Chuang, Y.; Hussain, Z.; Pan, F.; Devereaux, T. P.; Yang, W. Spectroscopic Signature of Oxidized Oxygen States in Peroxides. *J. Phys. Chem. Lett.* **2018**, *9* (21), 6378–6384. https://doi.org/10.1021/acs.jpclett.8b02757.

(28) Wu, J.; Zhuo, Z.; Rong, X.; Dai, K.; Lebens-Higgins, Z.; Sallis, S.; Pan, F.; Piper, L. F. J.; Liu, G.; Chuang, Y.; Hussain, Z.; Li, Q.; Zeng, R.; Shen, Z.; Yang, W. Dissociate Lattice Oxygen Redox Reactions from Capacity and Voltage Drops of Battery Electrodes. *Sci.*

Adv. **2020**, *6* (6), eaaw3871. https://doi.org/10.1126/sciadv.aaw3871.

(29) Dai, K.; Wu, J.; Zhuo, Z.; Li, Q.; Sallis, S.; Mao, J.; Ai, G.; Sun, C.; Li, Z.; Gent, W. E.; Chueh, W. C.; Chuang, Y.; Zeng, R.; Shen, Z.; Pan, F.; Yan, S.; Piper, L. F. J.; Hussain, Z.; Liu, G.; Yang, W. High Reversibility of Lattice Oxygen Redox Quantified by Direct Bulk Probes of Both Anionic and Cationic Redox Reactions. *Joule* **2019**, *3* (2), 518–541. https://doi.org/10.1016/j.joule.2018.11.014.

(30) Clément, R. J.; Xu, J.; Middlemiss, D. S.; Alvarado, J.; Ma, C.; Meng, Y. S.; Grey, C. P. Direct Evidence for High Na+ Mobility and High Voltage Structural Processes in P2-Nax[LiyNizMn1-y-z]O2 (x, y, z ≤ 1) Cathodes from Solid-State NMR and DFT Calculations. *J. Mater. Chem. A* **2017**, *5* (8), 4129–4143. https://doi.org/10.1039/c6ta09601h.

(31) Chen, Q.; Pei, Y.; Chen, H.; Song, Y.; Zhen, L.; Xu, C. Y.; Xiao, P.; Henkelman, G. Highly Reversible Oxygen Redox in Layered Compounds Enabled by Surface Polyanions. *Nat. Commun.* **2020**, *11* (1), 3411. https://doi.org/10.1038/s41467-020-17126-3.

(32) Cao, X.; Li, X.; Qiao, Y.; Jia, M.; Qiu, F.; He, Y.; He, P.; Zhou, H. Restraining Oxygen Loss and Suppressing Structural Distortion in a Newly Ti-Substituted Layered Oxide P2-$Na_{0.66}Li_{0.22}Ti_{0.15}Mn_{0.63}O_2$. *ACS Energy Lett.* **2019**, *4* (10), 2409–2417. https://doi.org/10.1021/acsenergylett.9b01732.

(33) Li, C.; Zhao, C.; Hu, B.; Tong, W.; Shen, M.; Hu, B. Unraveling the Critical Role of Ti Substitution in P2-NaxLiyMn1-yO2 Cathode for Highly Reversible Oxygen Redox Chemistry. *Chem. Mater.* **2020**, *32* (3), 1054–1063. https://doi.org/10.1021/acs.chemmater.9b03765.

(34) Zhang, K.; Kim, D.; Hu, Z.; Park, M.; Noh, G.; Yang, Y.; Zhang, J.; Lau, V. W.; Chou, S.-L.; Cho, M.; Choi, S.-Y.; Kang, Y.-M. Manganese Based Layered Oxides with Modulated Electronic and Thermodynamic Properties for Sodium Ion Batteries. *Nat. Commun.* **2019**, *10* (1), 5203. https://doi.org/10.1038/s41467-018-07646-4.

(35) Günter, F. J.; Habedank, J. B.; Schreiner, D.; Neuwirth, T.; Gilles, R.; Reinhart, G. Introduction to Electrochemical Impedance Spectroscopy as a Measurement Method for the Wetting Degree of Lithium-Ion Cells. *J. Electrochem. Soc.* **2018**, *165* (14), A3249–A3256. https://doi.org/10.1149/2.0081814jes.

(36) Rahman, M. M.; Mao, J.; Kan, W. H.; Sun, C.-J.; Li, L.; Zhang, Y.; Avdeev, M.; Du, X.-W.; Lin, F. An Ordered P2/P3 Composite Layered Oxide Cathode with Long Cycle Life in Sodium-Ion Batteries. *ACS Mater. Lett.* **2019**, *1* (5), 573–581. https://doi.org/10.1021/acsmaterialslett.9b00347.

Graphical abstract

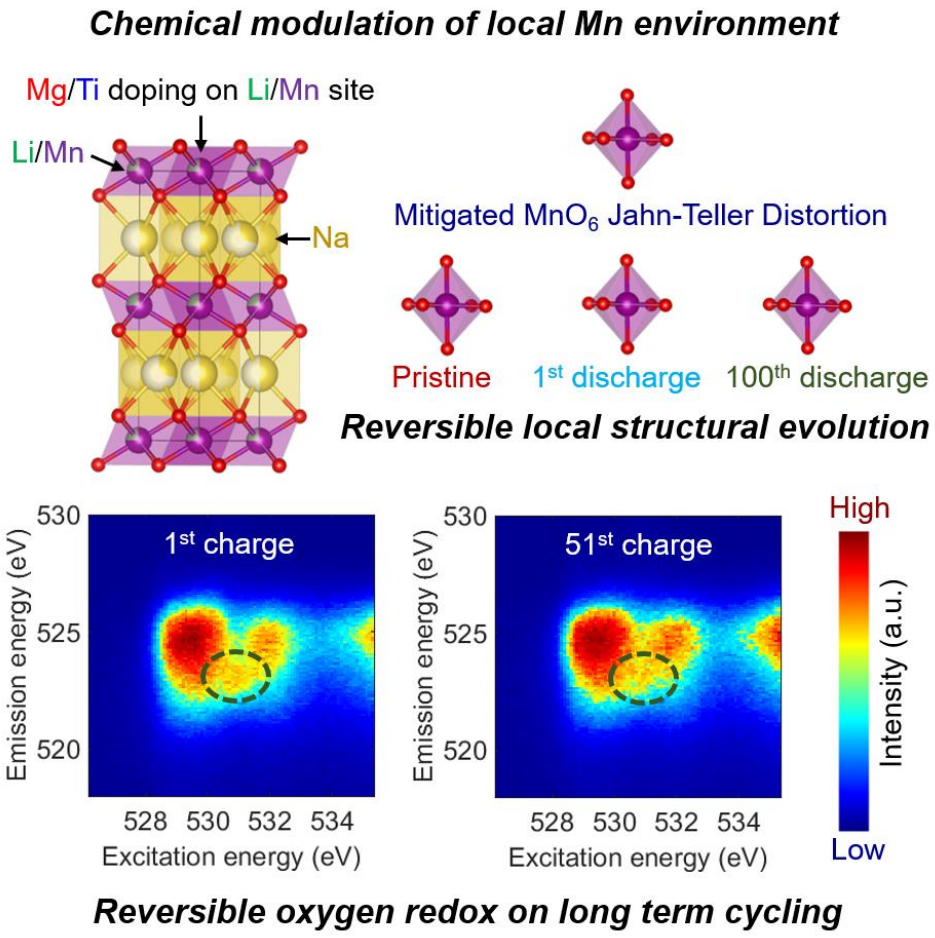

Supporting information for:

Chemical modulation of local transition metal environment enables reversible oxygen redox in Mn-based layered cathodes

Muhammad Mominur Rahman,[1] Scott McGuigan,[1] Shaofeng Li,[2] Lina Gao,[3] Dong Hou,[1] Zhijie Yang,[1] Zhengrui Xu,[1] Cheng-Jun Sun,[4] Jue Liu,[5] Xiaojing Huang,[6] Xianghui Xiao,[6] Yong Chu,[6] Sami Sainio,[2] Dennis Nordlund,[2] Xueqian Kong,[3] Yijin Liu,[2] and Feng Lin[1]*

1. Department of Chemistry, Virginia Tech, Blacksburg, VA 24061, USA
2. Stanford Synchrotron Radiation Lightsource, SLAC National Accelerator Laboratory, Menlo Park, CA 94025, USA
3. Department of Chemistry, Zhejiang University, Hangzhou, Zhejiang 310027, China
4. Advanced Photon Source, Argonne National Laboratory, Argonne, IL 60439, USA
5. Oak Ridge National Laboratory, Oak Ridge, TN 37830, USA
6. National Synchrotron Light Source II, Brookhaven National Laboratory, Upton, NY 11973, USA

Email: fenglin@vt.edu

Materials and methods

Material synthesis. $Na_xLi_yMn_{1-y}O_2$ was synthesized with stoichiometric amount of Na_2CO_3, LiOH, and Mn_2O_3. The precursors were ball milled at a rate of 2100 rpm for 6 hours. The mixed precursor was calcined in a box furnace under air atmosphere at 700 ºC for 10 hours followed by rapid quenching. For rapid quenching, the material was poured on a Cu plate placed in a sand bath and allowed to cool down to room temperature. The material was preserved in a scintillation vial filled with Ar for future use. The precursor of Mg/Ti dual doped $Na_xLi_yMn_{1-y}O_2$ was synthesized from the precipitation of a solution of $MnSO_4.H_2O$, $MgSO_4.7H_2O$, and titanium oxysulfate solution. The salt solutions were precipitated to a mixed metal hydroxide by adding a basic solution of $NaOH/NH_4OH$ (1.2:1 molar ratio). The reaction was performed in a nitrogen environment. The precipitate was filtered and dried in a vacuum oven overnight at 120 ºC. The mixed metal hydroxide precipitate was mixed with a stoichiometric amount of Na_2CO_3 and LiOH. The precursor was calcined in a box furnace under an air atmosphere at 700 ºC and 850 ºC for 10 hours. The calcined material was cooled down either by rapid quenching as described earlier or by letting the heated material cool down naturally inside the box furnace after the heating was completed. The calcined material was stored in an Ar filled scintillation vial for further use.

Electrochemical characterization. Composite electrodes of $Na_xLi_yMn_{1-y}O_2$ and Mg/Ti doped $Na_xLi_yMn_{1-y}O_2$ were made from 80% active material, 15% carbon black, and 5% polyvinylidene difluoride (PVDF) as the binder. A slurry was made with the aforementioned components by utilizing N-methyl-2-pyrrolidone as the solvent to dissolve PVDF. The slurry was casted on a carbon coated aluminum foil by the Doctor blade method, dried in vacuum oven at 120 ºC overnight, cut into disks of 10 mm diameter, and stored in the glovebox. The Na cells were assembled with $Na_xLi_yMn_{1-y}O_2$ composite electrode and Mg/Ti doped $Na_xLi_yMn_{1-y}O_2$ composite

electrode as cathodes, Na metal as the anode, Whatman glass fiber (1827-047934-AH) as the separator, and 0.56 M $NaPF_6$ in propylene carbonate (containing 2 volume% fluoroethylene carbonate additive) as the electrolyte. Cycling was performed at C/10 rate (18 mA/g current density) and 1C rate (180 mA/g current rate) using Wuhan Land battery cyclers. Kinetic measurement through galvanostatic intermittent titration technique (GITT) was performed on Wuhan LAND battery cycler by applying a 1-hour constant current pulse at C/10 rate followed by open cell relaxation for 10 hours until the voltage reaches to 4.5 V during the charging process or 1.5 V during the discharging process. The apparent diffusion coefficient of Na^+ was calculated through the following formula:

$$\widetilde{D} = \frac{4}{\pi\tau}\left(\frac{m_B V_M}{M_B S}\right)^2 \left(\frac{\Delta E_S}{\Delta E_t}\right)^2$$

Where, $\widetilde{D}$ is the Na^+ diffusion coefficient (cm^2/s), τ is the duration of the constant current pulse (s), m_B is the mass of the active component of the cathode (g), M_B is the molar mass of the active component of the cathode (g), V_M is molar volume (cm^3/mol), S is the contact area of the electrode and the electrolyte (cm^2), ΔE_S is the steady state voltage change due to the constant current pulse, and ΔE_t is the voltage change during the constant current pulse, excluding the iR drop.

Materials characterization. XRD patterns of the materials were collected on a benchtop Rigaku Miniflex II diffractometer working on a Cu Kα radiation of 1.54 Å wavelength. A step size of 0.02º and a scanning rate of 1º/min were utilized to acquire the patterns. Morphology of the materials was evaluated using LEO 1550 scanning electron microscope operated at a 5.0 kV accelerating voltage. SEM-EDS imaging was performed on FEI Quanta 600 FEG scanning electron microscope with Bruker EDX detector operating at a voltage of 20 kV. Polishing method was utilized to expose the bulk of the particle for SEM-EDS analysis. The particles were dispersed in epoxy resin and

dried overnight for solidification. After the epoxy was hardened, it was polished with sandpaper to remove the surface region and expose the bulk of the particles. Elemental quantification in pristine material and transition metal dissolution in electrolyte was performed through Thermo Electron iCAP-RQ inductively coupled plasma mass spectrometer (ICP-MS). 3D tomographic images were acquired in hard X-ray nanoprobe beamline at National Synchrotron Lightsource II. X-ray beam of 9.6 keV energy and 60 nm spot size was utilized to acquire images. The voxel size of the 3d images was 30 nm x 30 nm x 30 nm. Image reconstruction was performed in an open-source code called TomoPy. Soft XAS measurements are performed in beamline 10-1 at Stanford synchrotron Radiation Lightsource. Measurement was conducted at ultrahigh vacuum condition (10^{-9} Torr) at room temperature. A ring current of 350 mA and a 1000 $l.mm^{-1}$ grating monochromator were utilized for data collection. Data was collected at total electron yield (TEY) mode by collecting the sample drain current and in fluorescence yield more (FY) with a silicon diode. Samples were loaded on an aluminum sample stick with double sided tape. A nitrogen filled glovebag was used for sample transfer to minimize exposure to air. Hard X-ray measurement (Mn K-edge) was performed in beamline 20-ID at Advanced Photon Source (Argonne National Laboratory). Si(111) monochromator was utilized to monochromatize the beam. Mn K-edge spectra were acquired in the transmission mode. Oxygen resonant inelastic X-ray scattering is performed in the beamline 10-1 at Stanford Synchrotron Radiation Lightsource with a TES spectrometer.[1,2] The TES spectrometer is positioned at a 90º angle with respect to the incident X-ray. Ultrahigh vacuum condition (5E-9 Torr) was utilized for data acquisition. Exposure to air during sample transfer was minimized through a nitrogen-filled glovebag. The data calibration is performed through a reference sample containing C, N, and O. ^{7}Li magic angle spinning (MAS) NMR experiments were performed on a Bruker DMX 300 NMR spectrometer using Bruker 4.0

mm HX MAS probe. The samples were packed in 4.0 mm rotors in an argon filled glove box and were spun at 10 kHz for spectra acquiring. We employed the projection-MATPASS (pj-MATPASS) pulse sequence to obtain high-resolution spectra. The recycle delay was set to 0.01 s and the 90º pulse length was 2.56 μs. The ^{7}Li shift was referenced to solid LiCl at -1.11 ppm. Neutron diffraction (ND) was performed on Nanoscale Ordered Materials Diffractometer (NOMAD) BL-1B, Spallation Neutron Source (SNS) at Oak Ridge National Laboratory. About 0.2–0.3 g powder sample was loaded into the quartz capillary (3 mm) and each measurement took about 1 h. The refinement of neutron diffraction patterns was conducted using the software GSAS EXPGUI. For each sample, three histograms with different d-spacing range were used simultaneous for combined refinements. The average structure was first investigated by performing Pawley fits on the as collected ND data. For each Pawley fit the background terms, unit cell parameters, and peak profiles were refined. The results of the Pawley fit were used as starting models for the analysis using the Rietveld method where the scale factor, atomic positions and atomic displacement parameters were also refined. The instrument parameters were calibrated by refining a standard Si powder (SRM 640e from NIST).

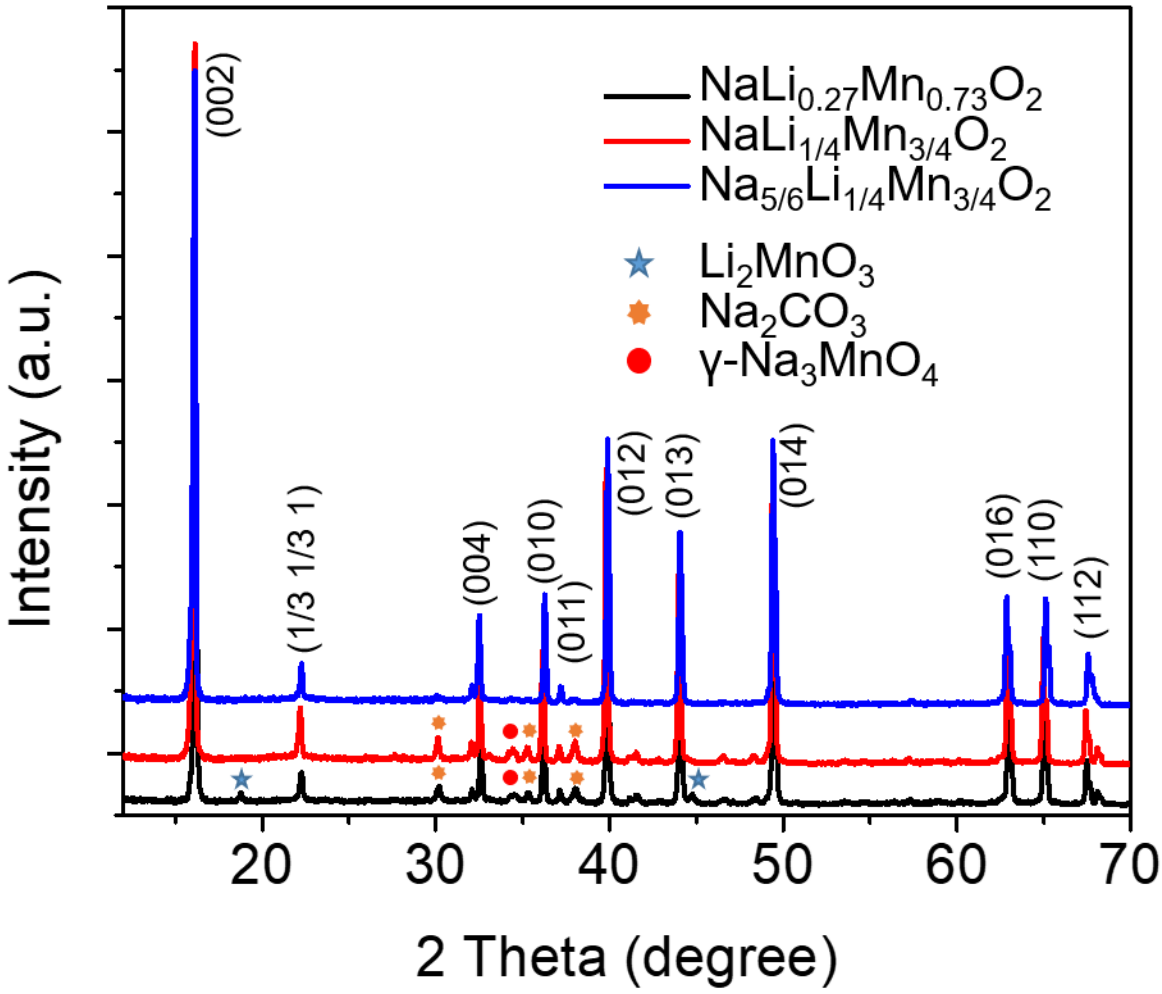

Figure S1. Figuring out the phase pure composition of $Na_xLi_yMn_{1-y}O_2$. X-ray diffraction (XRD) patterns of $Na_xLi_yMn_{1-y}O_2$ at various Na, Li, and Mn composition. Tuning the composition of $Na_xLi_yMn_{1-y}O_2$ to $Na_{5/6}Li_{1/4}Mn_{3/4}O_2$ can get rid of the impurity phases.[3]

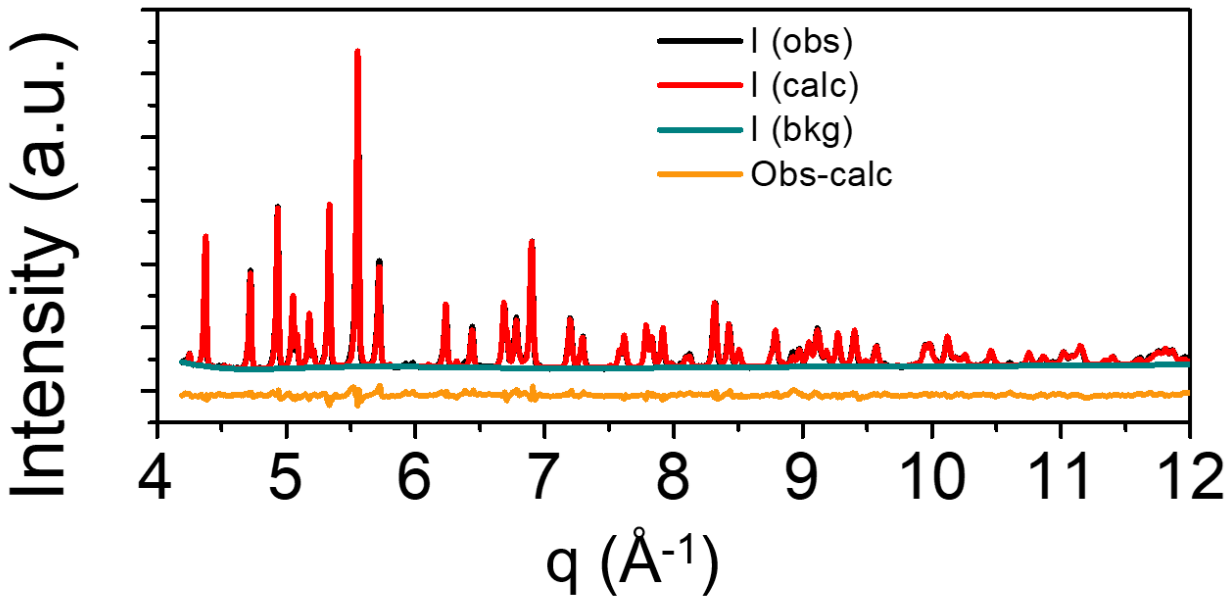

Figure S2. Crystal structure of phase pure $Na_xLi_yMn_{1-y}O_2$. Neutron diffraction pattern with Rietveld refinement of $Na_{5/6}Li_{1/4}Mn_{3/4}O_2$ (NLMO).

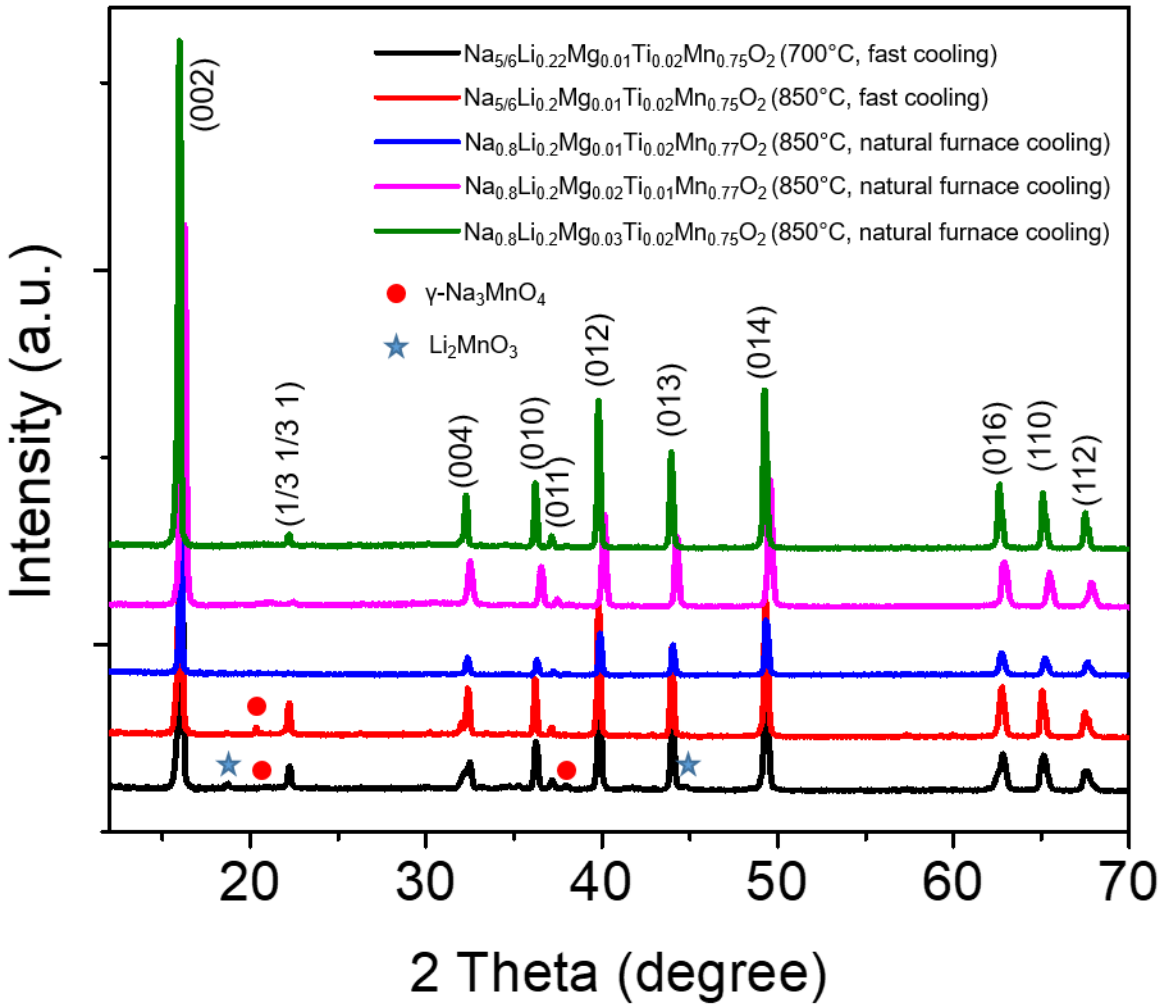

Figure S3. Figuring out the calcination condition and composition of phase pure Mg/Ti dual doped $Na_xLi_yMn_{1-y}O_2$. XRD patterns of Mg/Ti dual doped $Na_xLi_yMn_{1-y}O_2$ at various calcination condition and composition. The composition along with the calcination conditions (temperature and cooling procedure) are chosen based on the phase purity of the prepared material (minimizing the amount of impurity phases). A phase pure material can be obtained when the composition of the Mg/Ti dual doped $Na_xLi_yMn_{1-y}O_2$ is adjusted to $Na_{0.8}Li_{0.2}Mg_{0.03}Ti_{0.02}Mn_{0.75}O_2$, and calcination temperature to 850 ºC for 10 hours followed by natural furnace cooling.

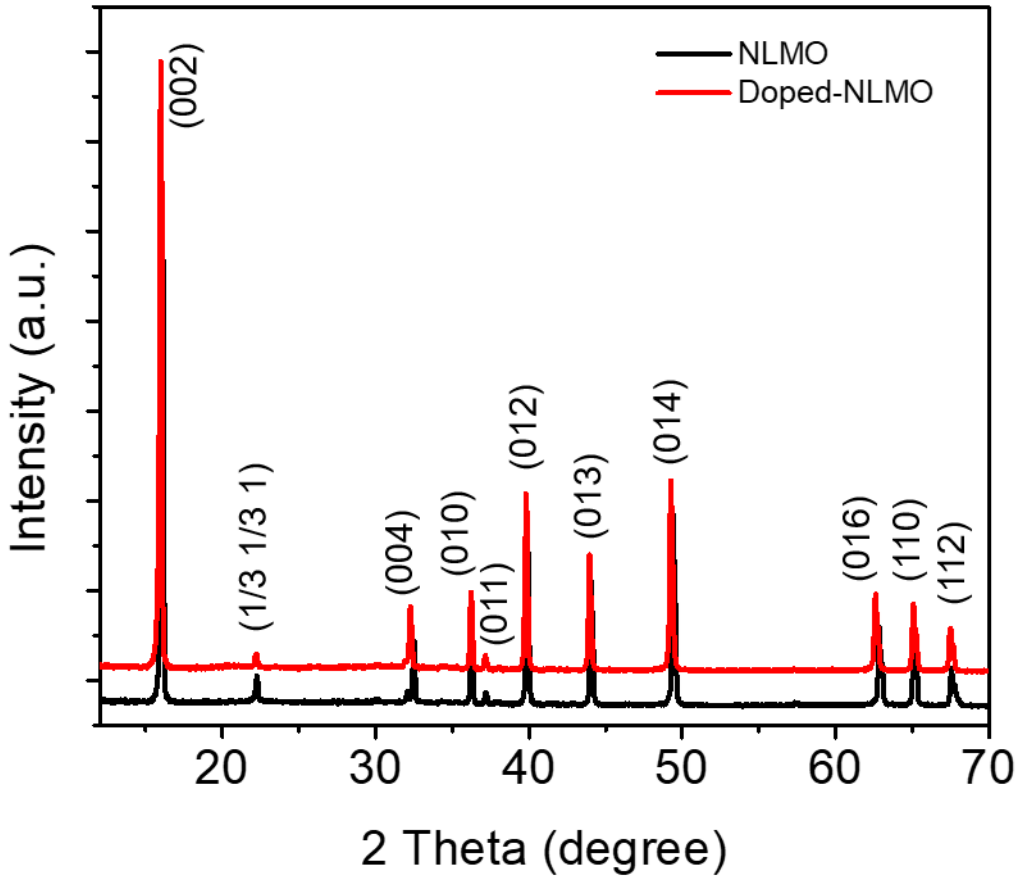

Figure S4. XRD pattern of phase pure $Na_{5/6}Li_{1/4}Mn_{3/4}O_2$ (NLMO), and $Na_{0.8}Li_{0.2}Mg_{0.03}Ti_{0.02}Mn_{0.75}O_2$ (doped-NLMO). All peaks in the pattern can be explained in terms of a hexagonal P2 phase with $P6_3/mmc$ space group. The superlattice reflection of the (1/3 1/3 1) plane originates from the Li/Mn honeycomb ordering in the transition metal layer.[3,4]

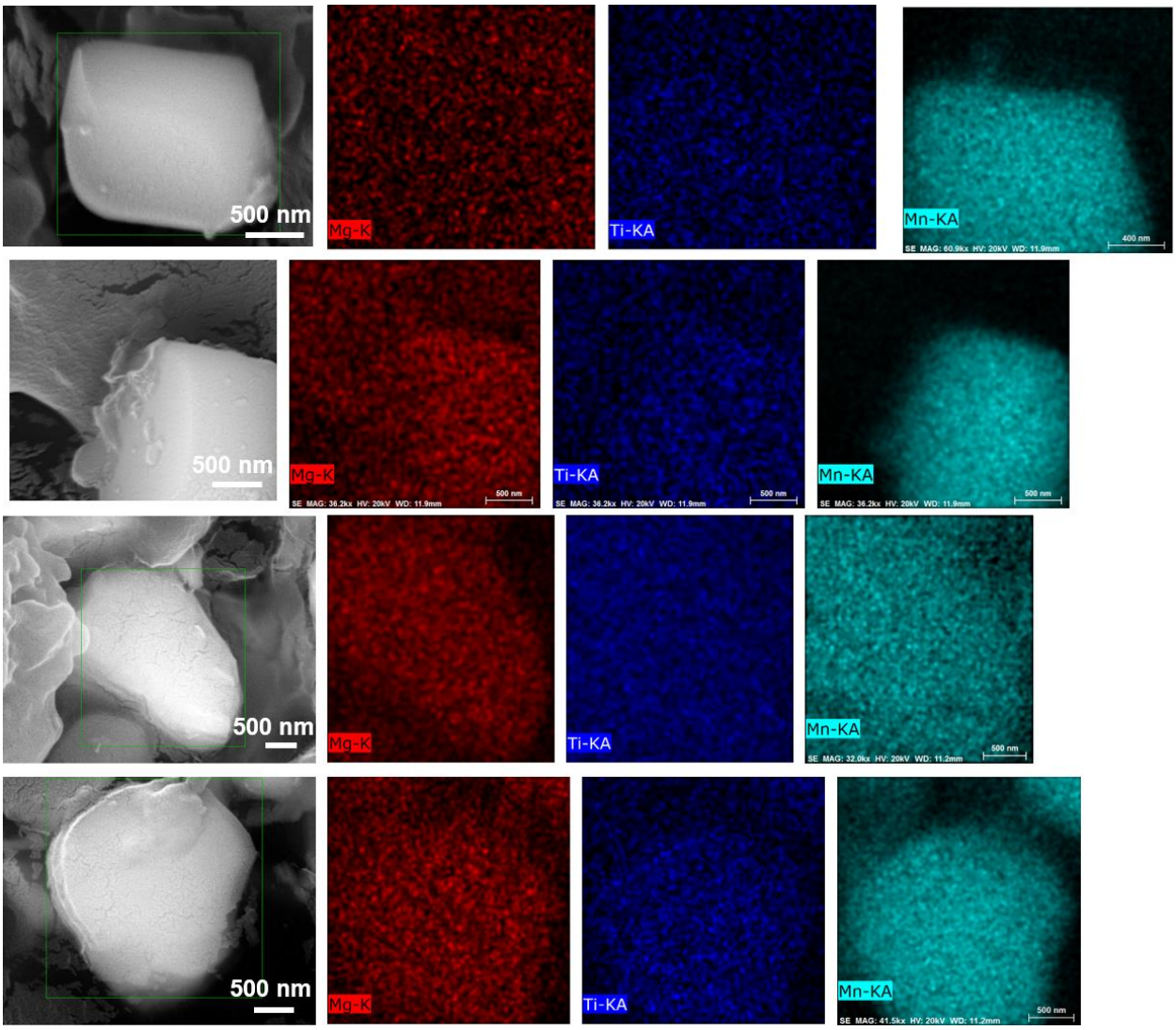

Figure S5. Dopant distribution (Mg and Ti) in doped-NLMO. SEM-EDS images of the exposed bulk of the doped-NLMO particles. The bulk of the doped-NLMO particles was exposed by the polishing method as explained in the "Materials and methods" section.

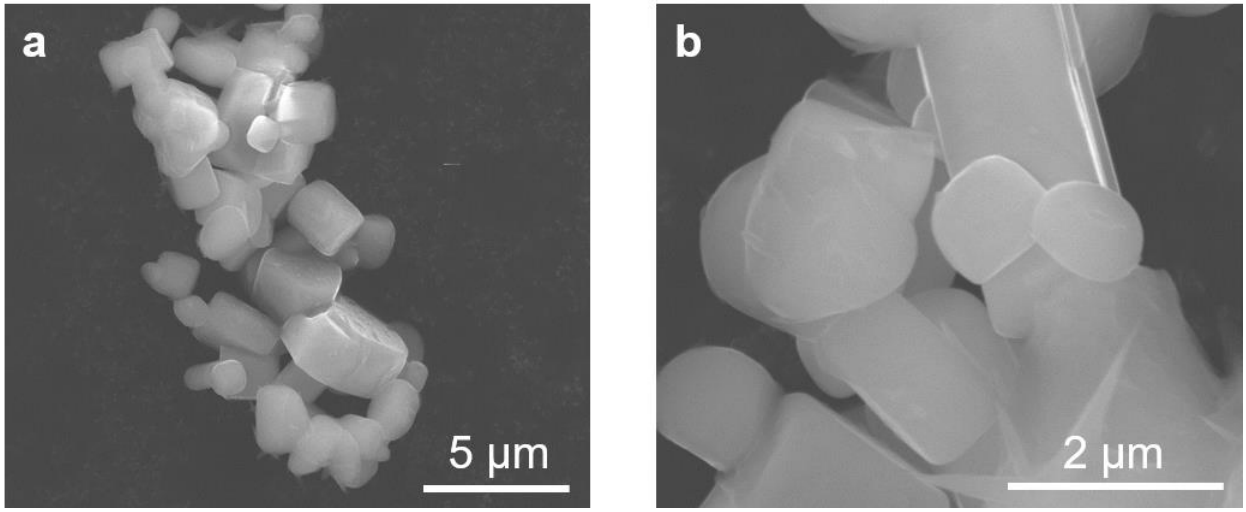

Figure S6. Morphology of NLMO at different magnifications (a-b).

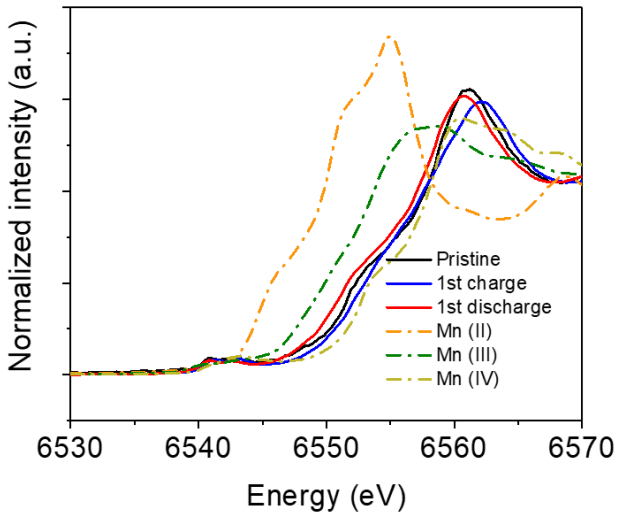

Figure S7. Charge compensation mechanism of NLMO. Mn K-edge XANES spectra of NLMO at different states of charge in the first cycle. Mn K-edge XANES spectra of three standards with Mn in +2 oxidation state (MnO), +3 oxidation state (Mn_2O_3), and +4 oxidation state (MnO_2) are included to evaluate the change in oxidation state of Mn in NLMO. The cycling is performed at C/10 rate.

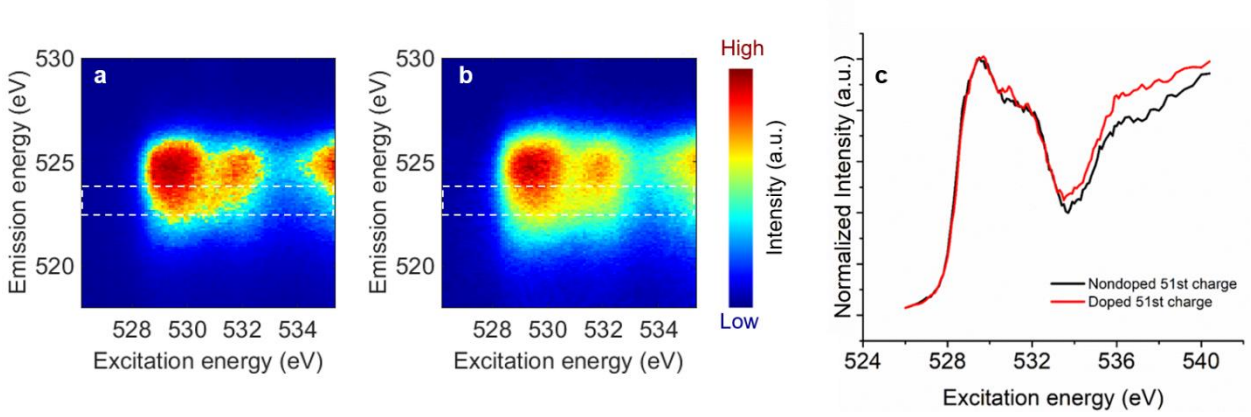

Figure S8. Oxygen redox reversibility in NLMO and doped-NLMO. (a) Oxygen K-edge resonant inelastic X-ray scattering (O RIXS) map of doped-NLMO after 51st charge. (b) O K-edge RIXS map of NLMO after 51st charge. (c) Excitation spectra of doped-NLMO and NLMO derived from the integration of the signal in the vertical direction along the white boxed region in (a-b). Cycling is performed at 1C rate for 50 cycles followed by charging at C/10 rate at 51st charge.

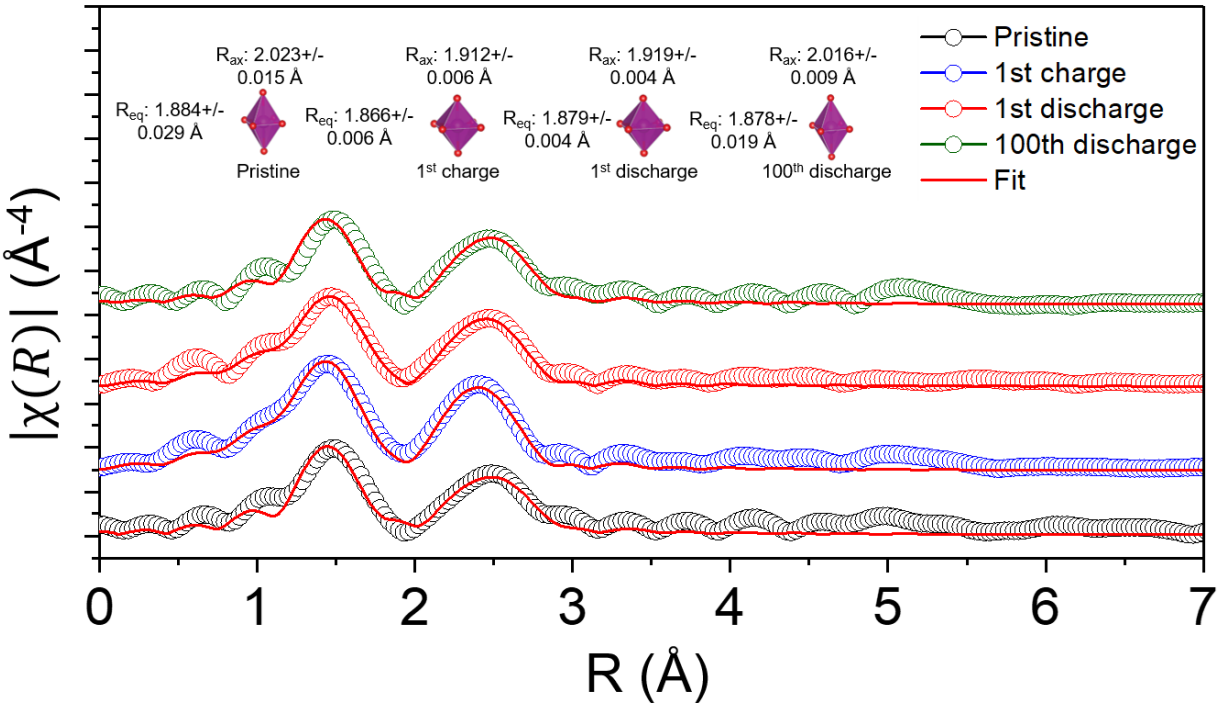

Figure S9. Quantification of the local Mn structural evolution in NLMO during electrochemical cycling. Magnitude of the fitted Mn K-edge EXAFS spectra at different stages of cycling. Cycling is performed at C/10 rate.

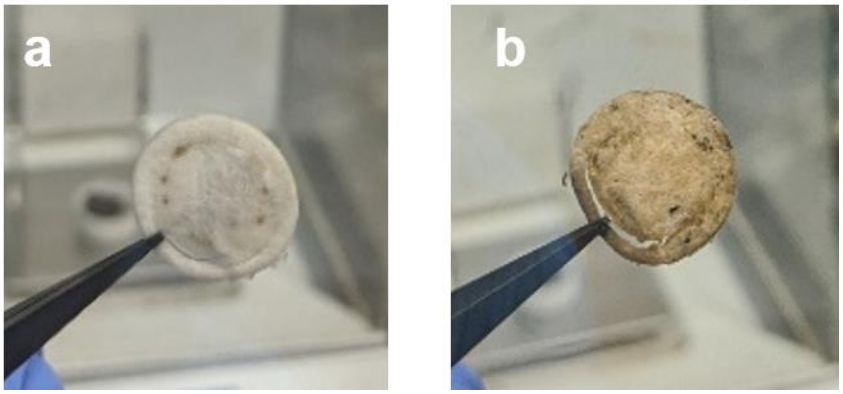

Figure S10. Change in appearance of the separator after electrochemical cycling. (a) Separator from the Na cell containing the doped-NLMO cathode cycled for 100 cycles at C/10 rate, and (b) separator from the Na cell containing the NLMO cathode cycled for 100 cycles at C/10 rate. Separator from the cycling of NLMO changes more in appearance than the separator from doped-NLMO.

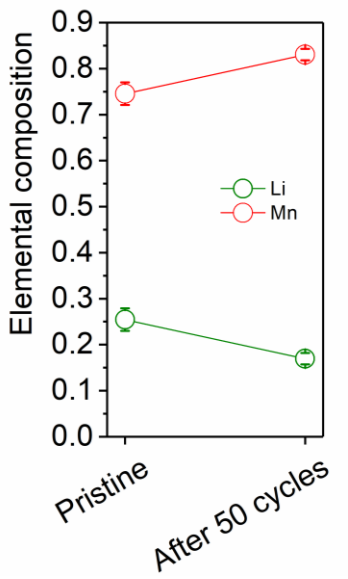

Figure S11. Li retention in NLMO after electrochemical cycling. Quantification of Li at pristine state and after cycling for 50 cycles at C/5 rate through ICP-MS.

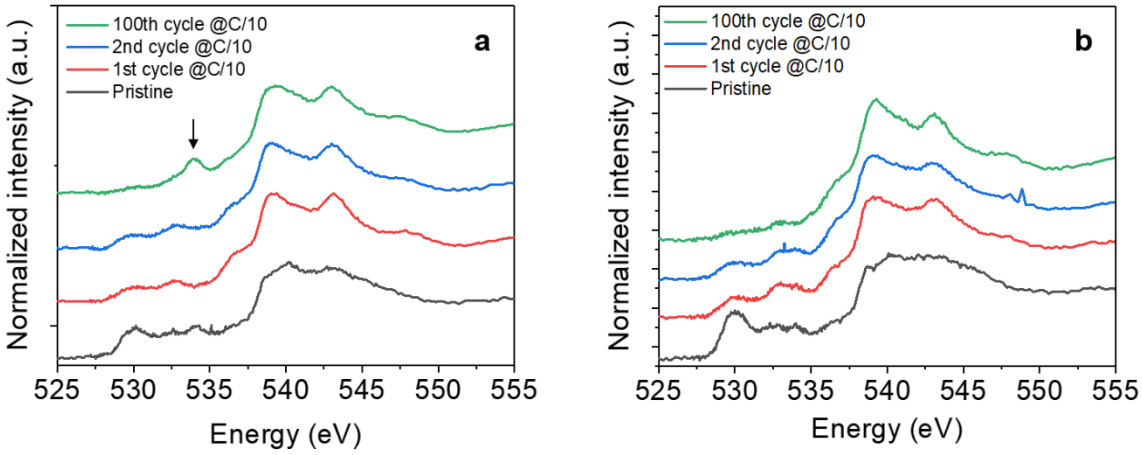

Figure S12. Evolution of subsurface TM 3d–O 2p hybridization during electrochemical cycling. (a) O K-edge spectra in fluorescence yield (FY) mode of NLMO at different stages of electrochemical cycling at C/10 rate. The peak marked by an arrow indicates the appearance of a carbonate and/or bicarbonate species. (b) O K-edge spectra in FY mode of doped-NLMO at different stages of cycling at C/10 rate.

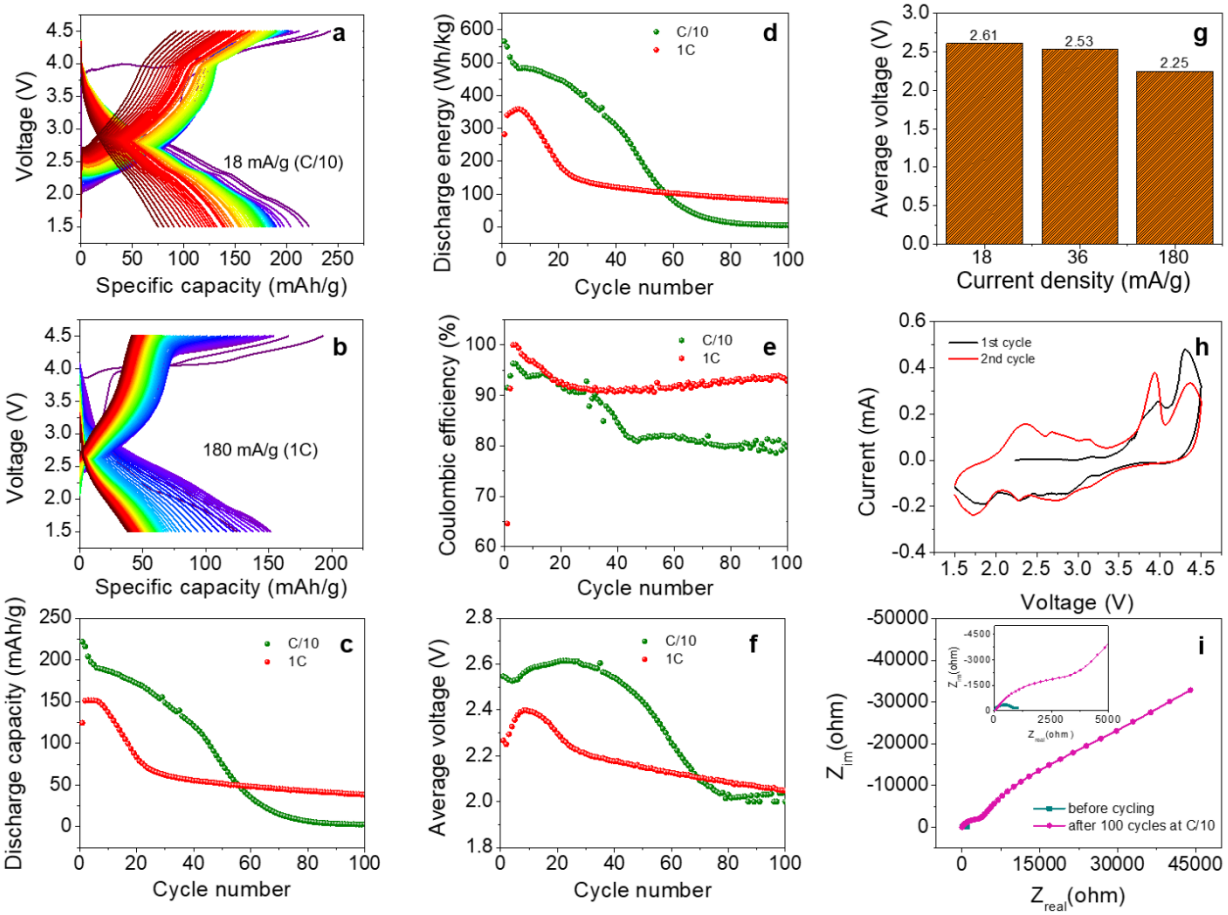

Figure S13. Electrochemical characterization of NLMO. (a) Charge and discharge curves of the Na cell containing NLMO as the cathode at C/10 rate for up to 50 cycles, (b) charge and discharge curves of the Na cell containing NLMO as the cathode at 1C rate for up to 200 cycles , (c) capacity retention against the cycle number at C/10 and 1C, (d) energy retention against the cycle number at C/10 and 1C, (e) Coulombic efficiency against the cycle number at C/10 and 1C, (f) average voltage against the cycle number at C/10 and 1C, (g) average voltage delivered by the Na cell containing the NLMO cathode at various current rates, (h) first and second cycle CV curves of NLMO (scan rate: 0.1 mV/s within 1.5-4.5 V) , and (i) Nyquist plot of the Na cell containing NLMO electrode before cycling and after 100 cycles at C/10 rate.

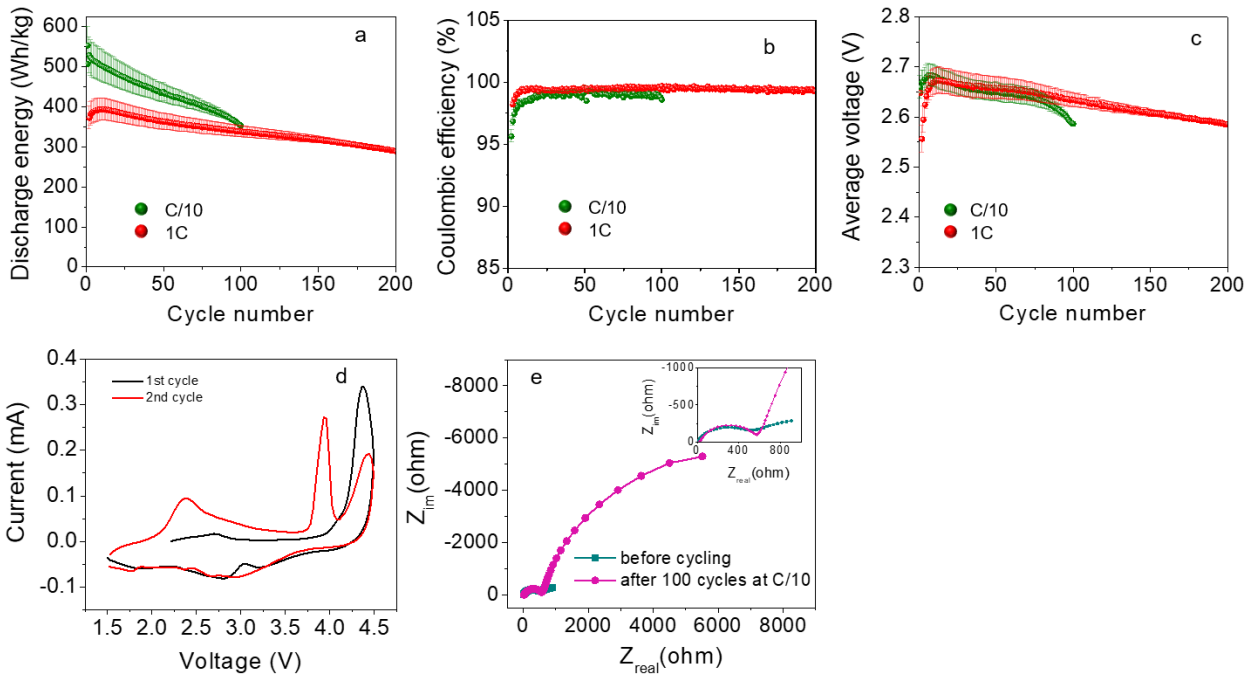

Figure S14. Electrochemical performance of doped-NLMO. (a) Energy density delivered by doped-NLMO against the cycle number at C/10 and 1C rate, (b) Coulombic efficiency delivered by the cell containing doped-NLMO as the cathode at C/10 and 1C rate, (c) average voltage delivered by doped-NLMO against the cycle number at C/10 and 1C rate, (d) first and second cycle cyclic voltammetry (CV) curves of doped-NLMO. The scan was performed at 0.1 mV/s rate within 1.5-4.5 V, and (e) Nyquist plots of the Na cells containing doped-NLMO as the cathode material before cycling and after cycling for 100 cycles at C/10 rate.

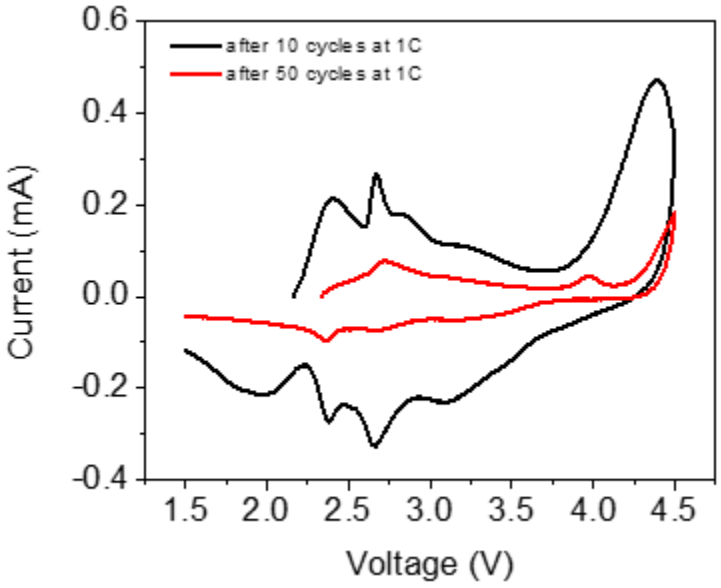

Figure S15. Cyclic voltammetry (CV) curves of NLMO after cycling for 10 cycles and 50 cycles at 1C in a Na cell containing the NLMO cathode. Scanning is performed at 0.1 mV/s rate within the voltage range of 1.5-4.5 V.

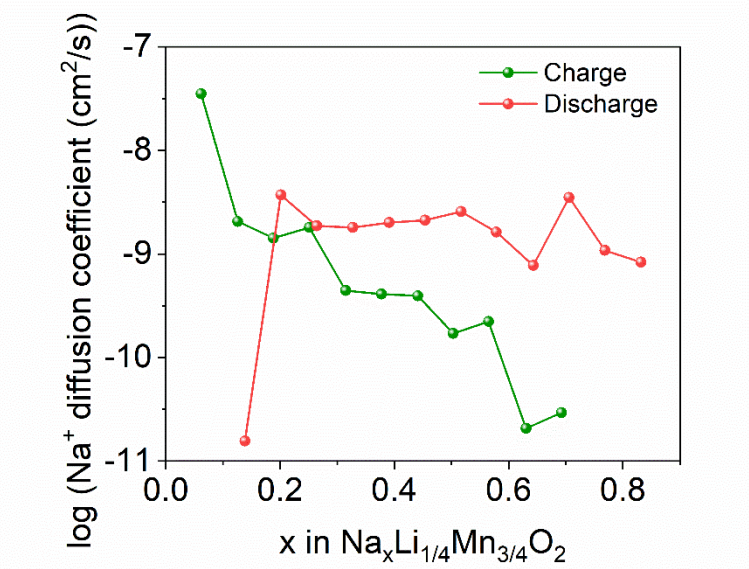

Figure S16. Electrochemical kinetics evaluation of NLMO. Na^+ diffusion coefficients measured from GITT. GITT was performed with 1 hour constant current charging/discharging at C/10 rate followed by 10 hour open circuit relaxation.

Table S1. Lattice occupancy of the elements determined by the Rietveld refinement of the neutron powder diffraction pattern. TM stands for transition metal layer and Na stands for the interlayer space between the two transition metal layer in the P2-type structure (see Figure 1b for a schematic P2 type crystal structure).

Material	**Li_{Na}**	**Li_{TM}**	**Mg_{Na}**	**Mg_{TM}**	**Ti_{TM}**	**Ti_{Na}**	**wR_p**	**Chi^2**
NLMO	5%	20%	NA	NA	NA	NA	0.04	11.70
Doped-NLMO	0%	20%	0%	3%	2%	0%	0.08	16.53

Table S2. Absorber (Mn) to scatterer (O) distance in NLMO determined by the fitting of the EXAFS spectra.

	R_{ax} (axial TM–O) (Å)	**R_{eq} (equatorial TM–O) (Å)**	**σ^2 (Deby-Waller factor) (R_{ax}) ($Å^2$)**	**σ^2 (Deby-Waller factor) (R_{eq}) ($Å^2$)**	**R_{ax}/R_{eq}**	**R-factor**
Pristine	2.023+/-0.015	1.884+/-0.029	0.008+/-0.004	0.0002+/-0.003	1.07	0.055
1^{st} charge	1.912+/-0.006	1.866+/-0.006	0.009+/-0.002	0.002+/-0.002	1.02	0.011
1^{st} discharge	1.919+/-0.004	1.879+/-0.004	0.004+/-0.003	0.009+/-0.004	1.02	0.006
100^{th} discharge	2.016+/-0.009	1.878+/-0.019	0.007+/-0.003	0.001+/-0.002	1.07	0.047

Table S3. Quantification of transition metal dissolution after 100 cycles at C/10 determined by ICP-MS on the separator.

Elemental composition	Mn (ppb/mg-active material)
$Na_{5/6}Li_{1/4}Mn_{3/4}O_2$ (NLMO)	370.4
$Na_{0.8}Li_{0.2}Mg_{0.03}Ti_{0.02}Mn_{0.75}O_2$ (doped-NLMO)	69.4

Table S4. Absorber (Mn) to scatterer (O) distance in doped-NLMO determined by the fitting of the EXAFS spectra.

	R_{ax} (axial TM–O) (Å)	**R_{eq} (equatorial TM–O) (Å)**	**σ^2 (Deby-Waller factor) (R_{ax}) (Å^2)**	**σ^2 (Deby-Waller factor) (R_{eq}) (Å^2)**	**R_{ax}/R_{eq}**	**R-factor**
Pristine	1.927+/-0.005	1.885+/-0.005	0.008+/-0.002	0.002+/-0.002	1.02	0.019
1st charge	1.914+/-0.004	1.873+/-0.004	0.009+/-0.001	0.003+/-0.001	1.02	0.011
1st discharge	1.927+/-0.004	1.886+/-0.004	0.007+/-0.001	0.002+/-0.002	1.02	0.014
100th discharge	1.919+/-0.004	1.877+/-0.004	0.006+/-0.001	0.003+/-0.001	1.02	0.017

References

(1) Titus, C. J.; Baker, M. L.; Lee, S. J.; Cho, H. M.; Doriese, W. B.; Fowler, J. W.; Gaffney, K.; Gard, J. D.; Hilton, G. C.; Kenney, C.; Knight, J.; Li, D.; Marks, R.; Minitti, M. P.; Morgan, K. M.; O'Neil, G. C.; Reintsema, C. D.; Schmidt, D. R.; Sokaras, D.; Swetz, D. S.; Ullom, J. N.; Weng, T. C.; Williams, C.; Young, B. A.; Irwin, K. D.; Solomon, E. I.; Nordlund, D. L-Edge Spectroscopy of Dilute, Radiation-Sensitive Systems Using a Transition-Edge-Sensor Array. *J. Chem. Phys.* **2017**, *147* (21), 214201. https://doi.org/10.1063/1.5000755.

(2) Doriese, W. B.; Abbamonte, P.; Alpert, B. K.; Bennett, D. A.; Denison, E. V.; Fang, Y.; Fischer, D. A.; Fitzgerald, C. P.; Fowler, J. W.; Gard, J. D.; Hays-Wehle, J. P.; Hilton, G. C.; Jaye, C.; McChesney, J. L.; Miaja-Avila, L.; Morgan, K. M.; Joe, Y. I.; O'Neil, G. C.; Reintsema, C. D.; Rodolakis, F.; Schmidt, D. R.; Tatsuno, H.; Uhlig, J.; Vale, L. R.; Ullom, J. N.; Swetz, D. S. A Practical Superconducting-Microcalorimeter X-Ray Spectrometer for Beamline and Laboratory Science. *Rev. Sci. Instrum.* **2017**, *88* (5), 053108. https://doi.org/10.1063/1.4983316.

(3) Yabuuchi, N.; Hara, R.; Kajiyama, M.; Kubota, K.; Ishigaki, T.; Hoshikawa, A.; Komaba, S. New O2/P2-Type Li-Excess Layered Manganese Oxides as Promising Multi-Functional Electrode Materials for Rechargeable Li/Na Batteries. *Adv. Energy Mater.* **2014**, *4* (13), 1301453. https://doi.org/10.1002/aenm.201301453.

(4) House, R. A.; Maitra, U.; Jin, L.; Lozano, J. G.; Somerville, J. W.; Rees, N. H.; Naylor, A. J.; Duda, L. C.; Massel, F.; Chadwick, A. V.; Ramos, S.; Pickup, D. M.; McNally, D. E.; Lu, X.; Schmitt, T.; Roberts, M. R.; Bruce, P. G. What Triggers Oxygen Loss in Oxygen Redox Cathode Materials? *Chem. Mater.* **2019**, *31* (9), 3293–3300. https://doi.org/10.1021/acs.chemmater.9b00227.